IOPscience iopscience.iop.org

Home Search Collections Journals About Contact us My IOPscience

Optical manipulation of colloids and defect structures in anisotropic liquid crystal fluids

This article has been downloaded from IOPscience. Please scroll down to see the full text article.

2011 J. Opt. 13 044001

(http://iopscience.iop.org/2040-8986/13/4/044001)

View the table of contents for this issue, or go to the journal homepage for more

Download details:
IP Address: 128.138.65.186
The article was downloaded on 14/03/2012 at 18:06

Please note that terms and conditions apply.

IOP Publishing Journal of Optics

J. Opt. **13** (2011) 044001 (19pp) doi:10.1088/2040-8978/13/4/044001

REVIEW ARTICLE

Optical manipulation of colloids and defect structures in anisotropic liquid crystal fluids

R P Trivedi[1,2], **D Engström**[1,3] **and I I Smalyukh**[1,2,4,5]

[1] Department of Physics, University of Colorado at Boulder, CO 80309, USA
[2] Liquid Crystal Materials Research Center, University of Colorado at Boulder, CO 80309, USA
[3] Department of Physics, University of Gothenburg, SE-41296 Göteborg, Sweden
[4] Renewable and Sustainable Energy Institute, University of Colorado at Boulder, CO 80309, USA

E-mail: Ivan.Smayukh@colorado.edu

Received 11 May 2010, accepted for publication 2 July 2010
Published 4 March 2011
Online at stacks.iop.org/JOpt/13/044001

Abstract
Optical trapping in anisotropic fluids such as liquid crystals shows inherently different behavior compared to that in isotropic media. Anisotropic optical and visco-elastic properties of these materials result in direction-sensitive and polarization-dependent interaction of the focused laser beam with colloidal inclusions, defects and structures of long-range molecular order, providing new means of non-contact optical control. Optical trapping properties are further enriched by laser-induced realignment of the optical axis that can be observed in these liquid crystalline materials at relatively low trapping laser powers. Optical manipulation of particles and defects in these anisotropic fluids is of immense importance for their fundamental study and from the standpoint of technological applications such as light-directed colloidal self-assembly and generation of tunable photonic architectures in liquid crystals. We review the basic physical mechanisms related to optical trapping in anisotropic liquid crystalline fluids and demonstrate how it can be employed in quantitative studies of colloidal interactions and both topological and mechanical properties of defects.

Keywords: optical manipulation, liquid crystals, colloids, defects, laser tweezers

(Some figures in this article are in colour only in the electronic version)

1. Introduction

Liquid crystals (LCs) are materials usually composed of anisometrically shaped molecules imbricated to feature long-range orientational order with varying degrees of partial positional order [1, 2]. They combine properties of crystals and fluids in a unique way in that they show both viscous as well as elastic and anisotropic optical properties in their behavior. In particular, nematic liquid crystals comprise rod-shaped molecules, the average local orientation whereof is characterized by the director $\mathbf{N}(\mathbf{r})$. Optically, thus a uniformly aligned block of nematic LC is a uniaxial crystal with its optical axis along $\mathbf{N}(\mathbf{r})$. Liquid crystals, owing to their unique set of mechanical, electrical and optical properties, have been of both fundamental and technological interest. They have long been known to be important in displays and other electro-optic technological devices [3–17] like spatial light modulators (SLM) and non-mechanical beam steerers and are also important from a biological standpoint as lipids, viruses, membranes and cytoskeleton proteins form LC phases [18–28].

[5] Author to whom any correspondence should be addressed.

 © 2011 IOP Publishing Ltd Printed in the UK & the USA

Optical manipulation has achieved special interest in the studies of LCs both because of the immense experimental capabilities of optical tweezers to probe these systems at the micron scale [29–40] combined with the richness of phenomena observed in LC media, with as well as without the presence of colloidal inclusions. Various LC-based systems have been studied using optical tweezers such as colloidal dispersions in LCs [41–51], LC defects and director structures [52–56], defects in Langmuir monolayers [57–62] and LC droplets [63–72]. The most peculiar aspects that make optical manipulation in LC media different from that in isotropic media are the direction and polarization dependence of refractive index and optical reorientation (the so-called Freederickz transition) at sufficiently high optical intensities. The first of these effects (direction/polarization sensitivity) arises from local variations in $\mathbf{N}(\mathbf{r})$ due either to the presence of inclusions or director deformations caused by defect structures. This spatial variation in $\mathbf{N}(\mathbf{r})$ imparts to LCs a characteristic of a uniaxial crystal with a spatially varying optical axis, by creating a corresponding spatial variation in refractive index that is polarization-dependent. A beam of light focused at a point where the local $\mathbf{N}(\mathbf{r})$ is parallel to the polarization $\mathbf{P}$ 'sees' the extraordinary refractive index n_e. If $\mathbf{P}$ is orthogonal to $\mathbf{N}(\mathbf{r})$, the beam sees the ordinary index n_o, and the whole gamut of refractive indexes from n_o to n_e can be spanned for the intermediate orientations of $\mathbf{P}$ with respect to $\mathbf{N}(\mathbf{r})$ from 0° to 90°. The optical reorientation of $\mathbf{N}(\mathbf{r})$ (also the optical axis for uniaxial liquid crystals) is an optical analog of the voltage-induced reorientation of the optical axis that forms the basis for the modern liquid crystal display applications; the difference is that the electric field of the laser beams is strongly non-uniform and at optical frequencies. We will see that trapping below the threshold for optical realignment is qualitatively different from trapping above it.

The applications of optical trapping manipulation in LCs enable a number of fascinating experimental capabilities such as probing elasticity- and defect-mediated colloidal interaction forces and colloidal self-organization, study of defect topology and line tension properties, etc. Furthermore, optically manipulated defects, colloids and the study of local phase transitions may enable modeling of important processes encountered in other branches of science, such as the role of defects from the point of view of defect-mediated phase transition phenomena not only in condensed matter but also in cosmology and particle physics.

This review introduces the basics of optical trapping in anisotropic liquid crystal media as well as overviews of some of the successful applications in the context of research on anisotropic LC fluids and other soft materials. Although a large number of important relevant studies have focused on controlled particle rotation and manipulation of birefringent nano-and micro-sized crystals [73–76], LC droplets [63–72], particles with nonspherical shapes [77–80], islands in thin films [45], polymerized liquid crystal colloids dispersed in isotropic fluids and also optical generation of structures in LCs [81], they are outside the scope of this review, which focuses on an overview of the manipulation of various objects (particles, defects, structures, etc) in anisotropic LC host media. This review is organized in the following manner. Section 2 describes the experimental set-up of laser tweezers integrated with the confocal microscopy capable of 3D optical imaging. It also discusses the typical material systems used for trapping and manipulation and how their properties determine the nature of trapping. Section 3 deals with the intriguing nature and properties of optical trapping of spherical particles in anisotropic media (vis-à-vis isotropic ones) and how trapping of these particles leads to controlling their dynamics in a unique manner or probing interaction forces between such particles. In section 4, we discuss manipulation of defects in liquid crystals, which is achieved either via the assistance of a trapped spherical particle or directly with a focused laser beam. Section 5 describes the trapping of anisotropically shaped particles such as nanorods and how they can be used to probe structures and defects in liquid crystals. Section 6 gives a brief discussion on the effect of laser-induced optical realignment of $\mathbf{N}(\mathbf{r})$ in LCs on trapping. The concluding remarks are provided in section 7.

2. Experimental details

2.1. Materials

The optical characteristics of an LC medium that determine the quality and efficiency of optical trapping are the ordinary and extraordinary refractive indices, n_o and n_e, respectively, and the birefringence of the LC, $\Delta n = n_e - n_o$; these properties are provided in table 1 for various LC materials. n_o and n_e (along with the colloidal particle index, n_p) determine the refractive index contrast between the LC and the particle and also the range of indexes to work with (the LC's effective refractive index n_{eff} can be varied from n_o to n_e by tuning the polarization of the light beam and varying its propagation direction with respect to the optical axis). Birefringence can cause defocusing and depolarization of the trapping beam as it propagates inside a birefringent medium, often making optical trapping in anisotropic media more difficult than in isotropic fluids. Not surprisingly, one of the first LC media to be used for optical trapping and manipulation was the so-called lyotropic LC [52] formed by an aqueous solution of a surfactant, which is very weakly birefringent ($\Delta n \sim 0.01$). Nematic LC materials like ZLI-2806 ($\Delta n \sim 0.04$) and ZLI-3412 ($\Delta n \sim 0.08$) are more suited for efficient trapping; in these materials, optical manipulation as deep as tens of micrometers into the LC cell can be performed, which is a difficult task in a material with high Δn, e.g. 5CB ($\Delta n = 0.18$) [53]. Although high Δn plays a detrimental role in achieving precise calibration of trapping forces, a material with high Δn can still be used as long as the trap is utilized only as a manipulator and not as a delicate measurer of forces. The advantage of a material with high Δn is that it provides a wide range of polarization-dependent refractive index n_{eff} which, as we shall see, can be utilized for polarization control of trapping forces. To enable 3D imaging of the director structure using fluorescence confocal polarizing microscopy (FCPM), the LC material is doped with a dye such as N, N'-bis(2,5-di-tert-butylphenyl)-3,4,9,10-perylenedicarboximide (BTBP, Aldrich). The dye molecules

Table 1. Properties of studied nematic LCs.

Material/property	K_{11} (pN)	K_{22} (pN)	K_{33} (pN)	n_e	n_o	Δn
MLC-6609	17.2	7.51	17.9	1.551	1.473	0.078
ZLI-3412	14.1	6.7	15.5	1.558	1.479	0.079
MLC-6815	—	—	—	1.519	1.467	0.052
ZLI-2806	14.9	7.9	15.4	1.518	1.475	0.043
5CB	6.4	3	10	1.714	1.536	0.178
AMLC-0010	17.2	7.51	17.9	1.55	1.47	0.08
E7	11.1	6.4	17.1	1.746	1.521	0.225
λ-phage DNA-based LC [18, 49]	—	—	—	—	—	$\lvert\Delta n\rvert < 0.01$

are anisotropic in shape (resembling the LC molecules), so that they align along the local $\mathbf{N}(\mathbf{r})$ and thus give correct visualization of the local director when excited by a beam of polarized FCPM imaging light.

By doping the nematic LC host with a certain concentration of chiral molecules (chiral dopant), one can obtain a chiral nematic LC. The cholesteric phase of a chiral nematic LC (CNLC) is characterized by the equilibrium pitch of the helix, the distance over which the LC molecules twist by 360°, forming the ground state structure. The value of the pitch depends on the concentration as well as the so-called 'helical twisting power' (h_{HTP}) of the chiral dopant in the nematic host. The resultant pitch of the CNLC mixture is given by $p = 1/(h_{HTP} \times C_{chiral})$, where C_{chiral} is the concentration of the chiral dopant in the CNLC mixture.

The shape and physical properties of particles (such as their refractive index and surface treatment) play an important role in determining the trapping behavior. The chemical treatment of surfaces determines the so-called 'surface anchoring', i.e. whether the LC molecules lie tangential to the surface of the particle or perpendicular to it, as well as the ensuing structure of the $\mathbf{N}(\mathbf{r})$ field around the particle that strongly influences the trapping characteristics (as we shall discuss in detail in section 3). For example, particles made of melamine resin ($n_p = 1.68$) offer tangential alignment while silica particles (soda lime, $n_p = 1.51$) treated with N,N-dimethyl-n-octadecyl-3-aminopropyltrimethoxysilyl chloride (DMOAP) tend to align the LC molecules normal to the surface, and their optical trapping depends not only on the refractive indices of the particles and surrounding medium, but also on the structure of $\mathbf{N}(\mathbf{r})$ (=optical axis) induced by the colloidal inclusion in the anisotropic LC medium. Furthermore, trapping properties also depend on the orientation of $\mathbf{N}(\mathbf{r})$ far away from the colloidal inclusion, usually determined by surface treatment of the confining substrates. Planar unidirectional alignment is achieved, for example, by spin-coating thin layers of polyimide like PI-2555 (HD Microsystems, NJ, USA) on the substrate and rubbing it to fix the in-plane orientation of the alignment. Vertical alignment can be obtained by, for example, spin-coating a polyimide like JALS-204 (JSR, Japan) or treating the substrate with surfactants such as DMOAP and lecithin.

2.2. Set-up for the integrated 3D optical manipulation and imaging

An important necessity of optical manipulation in anisotropic fluids is to be able to visualize the ensuing changes in long-range molecular alignment as well as both the motion and transformation of defects. These goals are usually not achievable using regular optical microscopy observations; techniques capable of nondestructive optical imaging of $\mathbf{N}(\mathbf{r})$ (preferably in 3D) need to be utilized. Occasionally, when the spatial changes of $\mathbf{N}(\mathbf{r})$ have a 2D character, polarizing microscopy is capable of providing this information. In this case, the sample is simply placed between crossed polarizers and imaged in either transmission or reflection modes simultaneously with the laser manipulation of particles or defects. However, polarizing microscopy gives only a 2D representation of the variation of $\mathbf{N}(\mathbf{r})$, from which it is often impossible to elicit the actual structure of $\mathbf{N}(\mathbf{r})$ in 3D. Hence, to have an unambiguous visualization of the $\mathbf{N}(\mathbf{r})$ structure around a colloidal particle or a defect in liquid crystals, the use of a 3D imaging technique is imperative. Polarized excitation and detection incorporated into 3D microscopy techniques can be employed to visualize the director pattern with sub-micron resolution in 3D. Various forms of microscopy methods that can be used for this purpose include techniques such as FCPM [82, 83] and nonlinear optical microscopy techniques such as coherent anti-Stokes Raman scattering polarizing microscopy (CARS-PM) [4, 84, 85], sum frequency generation microscopy [86], second harmonic generation [87], three-photon self-fluorescence [88], two-photon fluorescence microscopy [89] and other less common techniques. Each of these 3D imaging approaches has its own distinct advantages and drawbacks, often giving complementary information about the studied samples. Here we provide an example of a system obtained by integrating FCPM and holographic optical tweezers, which allows 3D manipulation and imaging of the resultant changes in the LC director structure in 3D.

Figure 1 shows an integrated optical trapping set-up built around a fluorescence confocal polarizing microscope. The holographic optical trapping system is based on an electrically addressed liquid crystal spatial light modulator (LC-SLM), consisting of 512 pixels × 512 pixels of 15 μm × 15 μm size each. The SLM updates its whole pixel array with computer-controlled phase-only holograms at a refresh rate of 15 frames s^{-1}, thus yielding the desired spatiotemporal trap patterns and allowing real-time manipulation. The two telescopes in the optical train, one before and the other after the SLM, resize the beam to overfill, respectively, the active area of the SLM and the back-aperture of the microscope objective used for trapping. The holographic nature of the trapping system enables movement of traps and manipulated objects not only in the transverse plane but also

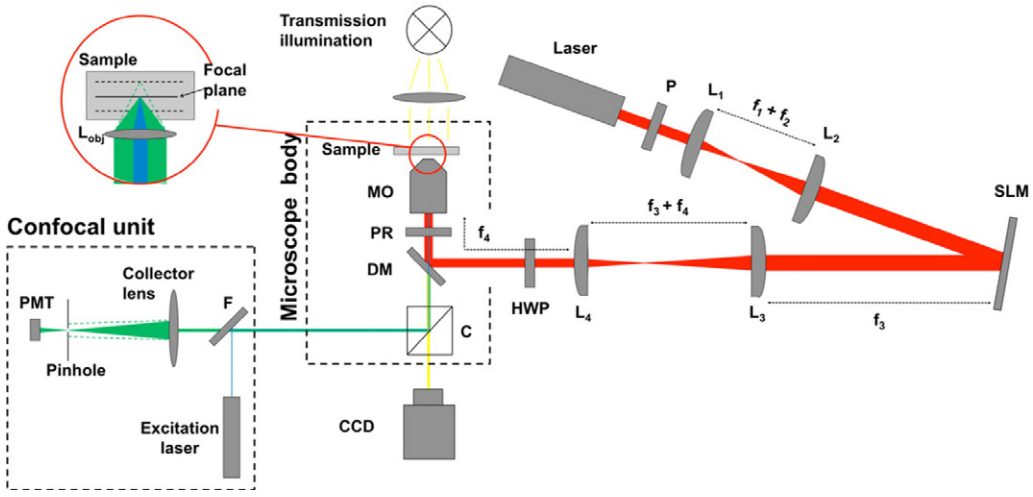

Figure 1. Integrated holographic optical trapping and confocal microscopy set-up. The trapping system is integrated with the inverted IX-81 microscope (Olympus) through the right-side laser port and contains: lenses L_1 (focal length $f_1 = 100$ mm), L_2 ($f_2 = 250$ mm), L_3 ($f_3 = 850$ mm) and L_4 ($f_4 = 400$ mm) which are plano-convex lenses with anti-reflection coating for 1064 nm; P is a glan-laser polarizer optimized for 1064 nm; SLM is the spatial light modulator; HWP is a half-waveplate; DM is the dichroic mirror; PR is a ferroelectric LC-based polarization rotator; MO is the microscope objective. The confocal excitation and detection unit integrated with the inverted microscope through the left-side port consists of five continuous-wave laser lines, a galvano-mirror scanning unit, filter bank and PMT-based fluorescence detection unit. C is a beamsplitting cube; F is a dichroic filter; PMT is a photomultiplier tube. L_{obj} represents the effective lens in the microscope objective.

along the microscope's optical axis. The computer-generated holographic technique also offers the use of novel types of beams like Laguerre–Gaussian beams having orbital angular momentum and a donut-shaped intensity profile. While the trapping is performed at 1064 nm, dye excitation lasers emitting at visible wavelengths (e.g. 488 nm excitation and 505–525 nm emission for the BTBP dye) are used to image the sample in 3D. The dichroic mirror allows simultaneous imaging and trapping using the same microscope objective. For a detailed description of the system and how its integrated features can be employed to achieve the desired goals of simultaneous manipulation and imaging, the reader is directed to [40, 51, 81].

3. Optical trapping and manipulation of colloids in liquid crystals

3.1. Director structure and refractive index corona around a particle

As discussed above in brief, the anisotropic material properties of the LC media influence the optical trapping properties. Even for spherical particles, one observes directional sensitivity of the trapping of colloidal particles in LCs, which arises mainly from the dependence of the effective refractive index (n_{eff}) 'seen' by the trapping beam on its linear polarization direction relative to the local director $\mathbf{N}(\mathbf{r})$. Local variations in $\mathbf{N}(\mathbf{r})$ surrounding the particle are determined by the surface treatment of the particles and the LC elasticity. Since $\mathbf{N}(\mathbf{r})$ is also the optical axis for uniaxial nematic LCs, these spatial variations cause the formation of anisotropic refractive index coronas (RICs) around the particles. The combined effects of particle's and LC's refractive indices, the surface treatment on the particle and the polarization of the trapping beam offer a rich parameter space for the control of laser trapping in LC media.

A spherical particle suspended in a nematic LC with uniform ground-state director $\mathbf{N}_0$ can form several kinds of director patterns (figure 2), depending on: (1) how its surface is treated to align the LC molecules and (2) the thickness of the cell relative to the particle size. This director pattern results in a refractive index shell around the particle—the polarization-dependent RIC. The equilibrium configuration of the director field is obtained by minimizing the elastic free energy in the presence of a particle with given surface boundary conditions. The Frank elastic energy cost of deformations for a nematic LC is given by [1]

$$F_{\text{elastic}} = \int_{\text{volume}} \left\{ \frac{K_{11}}{2}(\nabla \cdot \mathbf{N})^2 + \frac{K_{22}}{2}\left[\mathbf{N} \cdot (\nabla \times \mathbf{N}) + \frac{2\pi}{p}\right]^2 + \frac{K_{33}}{2}[\mathbf{N} \times (\nabla \times \mathbf{N})]^2 - K_{24}[\nabla \cdot [\mathbf{N}(\nabla \cdot \mathbf{N}) + \mathbf{N} \times (\nabla \times \mathbf{N})]] \right\} \mathrm{d}V \quad (1)$$

where K_{11}, K_{22}, K_{33} and K_{24} are elastic constants describing the splay, twist, bend and saddle-splay deformations, respectively. For a nematic LC, $2\pi/p = 0$ and the ground state with minimum free energy corresponds to a uniformly aligned state with $\mathbf{N}(\mathbf{r}) = \mathbf{N}_0$. For cholesteric LCs, the $2\pi/p \neq 0$ term renders a uniformly twisted state with pitch p as the stable ground state. The equilibrium director structure (obtained by minimizing the Frank elastic energy for given boundary conditions) can be used to obtain the RIC around the inclusion (in its equatorial plane) for two mutually orthogonal polarization directions, see figure 2.

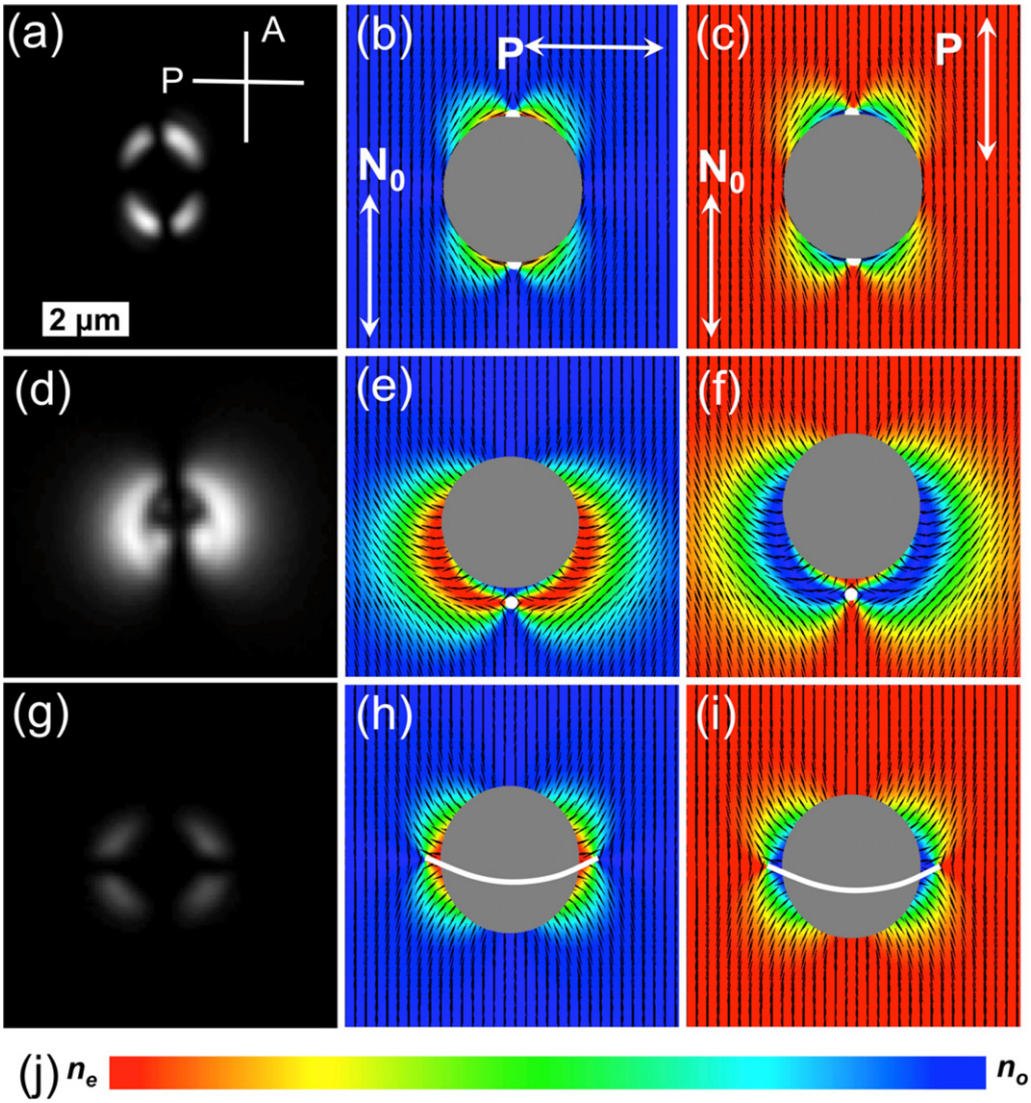

Figure 2. Colloidal particles with different surface anchoring forming various polarization-dependent refractive index coronas (RICs) in a nematic liquid crystal. (a) Polarizing microscopy texture under crossed polarizers for a particle with strong tangential surface anchoring that forms a quadrupolar $\mathbf{N}(\mathbf{r})$; the bars marked by 'P' and 'A' show orientations of the polarizer and the analyzer, respectively. ((b), (c)) Computer-simulated director structure around the bead and the resultant RIC for incident polarization $\mathbf{P}$ perpendicular to the far-field director $\mathbf{N}_0$ (b) and parallel to it (c). The surface defects called 'Boojums' are shown using white half-circles. (d) Polarizing microscopy image of a particle with strong homeotropic anchoring and the dipolar $\mathbf{N}(\mathbf{r})$ around it. ((e), (f)) Corresponding computer-simulated $\mathbf{N}(\mathbf{r})$ and the RICs for two orthogonal polarizations of a trapping beam; the point defect is marked by a filled white circle. (g) Polarizing microscopy texture for a particle with homeotropic anchoring showing quadrupolar symmetry of $\mathbf{N}(\mathbf{r})$ around it. ((h), (i)) Computer simulation of $\mathbf{N}(\mathbf{r})$ and RICs for two orthogonal polarizations; note the disclination ring formed around the particle in its equatorial plane. (j) Scale showing color coding of refractive index in the simulated images corresponding to the equatorial plane of the colloids. For more details, the reader is directed to [49]. (Colour online.)

By controlling the surface anchoring properties via surface treatment of the particles, one can obtain RICs having different symmetries. A spherical particle with tangential surface anchoring generates a quadrupolar molecular distortion around it with two surface point defects—boojums—at the poles of the particle along $\mathbf{N}_0$, see figures 2(a)–(c). When suspended in a cell much thicker than the particle size, a particle with its surface treated to align LC molecules perpendicular to the surface (homeotropic alignment) causes director deformation resembling that due to a point defect having topological charge $+1$. A point defect of topological charge -1 (a hyperbolic hedgehog) is formed in the bulk of the LC, creating a dipole with its axis aligned along $\mathbf{N}_0$, thus conserving the net topological charge of the system, see figures 2(d)–(f). A particle with homeotropic anchoring placed inside a cell with thickness comparable to the particle size gives rise to quadrupolar distortion from a disclination ring of strength $-1/2$ formed around the particle in its equatorial plane, see figures 2(g)–(i). A disclination ring of strength $-1/2$ is equivalent to a point defect of -1 charge, and so the net topological charge is conserved, balancing the virtual point defect of charge $+1$ created by the particle.

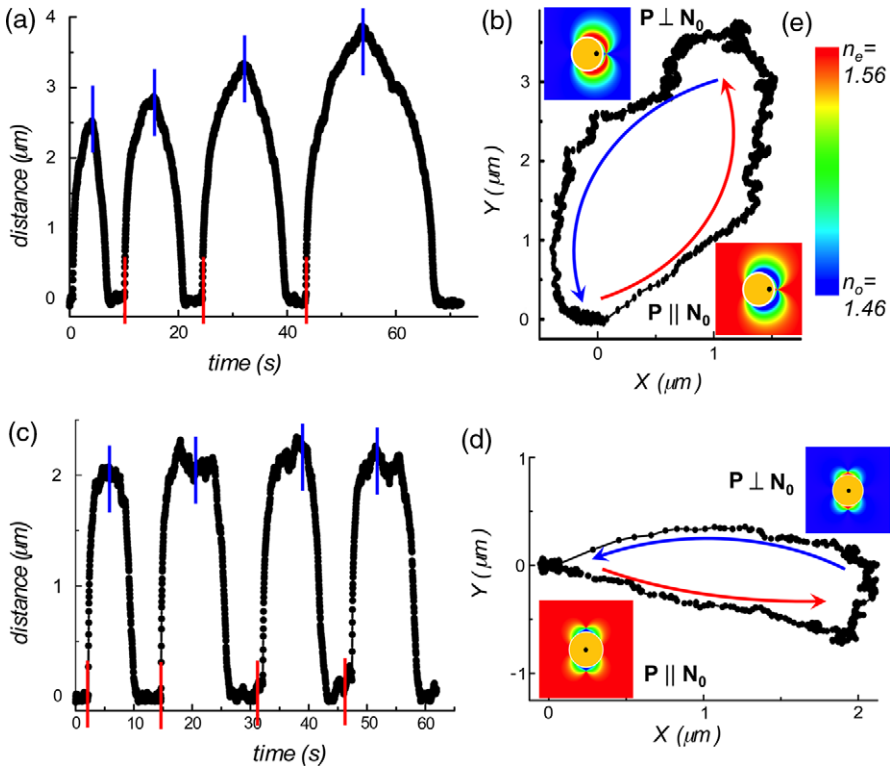

Figure 3. Polarization-controlled motion of colloidal particles in liquid crystals. (a) Distance (from the trap center) versus time for a dipolar particle as the polarization of the trap is switched repeatedly between two orthogonal states. The particle is repelled or attracted to the trap, depending on the laser beam's polarization direction. (b) Repulsive (arrow pointing away from the trap at $x = y = 0$, red online) and attractive (arrow pointing towards the trap position, blue online) motion trajectory for a dipolar particle as the polarization of the laser trap at $x = y = 0$ is switched between the two orthogonal states. (c) Distance (from the trap) versus time plot for a quadrupolar bead and (d) its trajectory of motion upon switching the linear polarization direction. The upper (blue online) time markers in (a) and (c) correspond to the instants when the polarization of light is switched to $\mathbf{P} \perp \mathbf{N}_0$ (attractive trapping potential), and the lower (red online) markers correspond to the instants when the polarization is switched to $\mathbf{P} \parallel \mathbf{N}_0$ (repulsive 'trapping' potential). (e) Color scale for the refractive index in (b) and (d). For details, see [49]. (Color online.)

The inclusion of particles breaks the symmetry by creating dipolar or quadrupolar patterns around them. The size of the distortions of $\mathbf{N}(\mathbf{r})$ and the RIC thus created is the largest for a dipolar particle. The director attains the far-field orientation along $\mathbf{N}_0$ at relatively smaller distances for quadrupolar colloids, see figures 2(a) and (g). The ensuing RICs are polarization-dependent in all of these cases. This polarization dependence allows for control of trapping properties. For example, a particle with refractive index $n_o < n_p < n_e$ experiences attractive trapping for certain polarizations (i.e. for $\mathbf{P} \perp \mathbf{N}_0$) but is repelled from the center of the trap for polarizations close to $\mathbf{P} \parallel \mathbf{N}_0$. Consistent with the size of the RIC around the bead, the interaction with the laser trap is felt furthest for dipolar particles (up to a distance $\cong 6R$, where R is the radius of the particle) and the least for quadrupolar beads (only for distances $\cong R$).

3.2. Polarization-dependent dynamics and anisotropy of laser trapping

In isotropic fluids, regardless of polarization, optical gradient forces have either an attractive or repulsive nature, depending on the contrast of refractive index between the particle and the surrounding medium. This is often not the case for laser manipulation of colloids dispersed in anisotropic LC fluids. For example, figure 3 shows how the motion of a particle is controlled only by switching the polarization of the trapping beam that allows for reversing the sign of the optical gradient force. Upon switching the polarization states, the particle is attracted into the trap or it recedes away from the trap, depending on the polarization state, see figures 3(a) and (c). Since the RIC is polarization-dependent and also depending on whether n_p is closer to n_e or n_o, the attractive and repulsive parts of the trajectories look different. The shape and orientation of trajectories (with respect to $\mathbf{N}_0$) for dipolar versus quadrupolar beads reflect the shape and symmetry of the RICs around those beads, see figures 3(b) and (d).

In isotropic fluids, spherical particles are trapped with their centers aligned along the optical axis, slightly shifted downstream due to the effect of scattering forces. In the case of anisotropic fluids, an interesting consequence of the RICs surrounding the beads and the polarization dependence of the effective refractive index value is that the bead is not always trapped with its center lying on the optical axis of the focused beam, see figure 4. Depending on the direction of approach of the trapping beam while shifting between the filled white dots in figure 4, it can be trapped along the axis of the elastic dipole, see figure 4—cases 1 and 3, or at a

high n_{eff} spot in the RIC wing (outside the particle). All the trapping locations are stable, even the ones outside the particle (figure 4—cases 2 and 4), as the high refractive index regions in the RIC are surrounded by low-index regions. Since the particle and the RIC are mechanically coupled to each other due to the LC elasticity, they follow each other when either the bead or RIC is translated using the laser trap. Another interesting consequence is the ability to manipulate particles with refractive index lower than the surrounding medium, i.e. even if $n_{\text{p}} < n_{\text{o}} < n_{\text{e}}$. There are two mechanisms at work under different scenarios: below the Freedericksz transition, the trapping is made possible by the RIC formed around the particle which has regions of higher refractive index surrounded by those of lower index. For a particle with dipolar $\mathbf{N}(\mathbf{r})$ and with n_{p} such that $n_{\text{e}} > n_{\text{o}} > n_{\text{p}}$, there are two stable trapping points outside of the particle for a laser's linear polarization orthogonal to $\mathbf{N}_0$. Thus even a particle with n_{p} lower than the surrounding medium can be trapped for certain laser polarizations because of the refractive index pattern that the bead creates around itself via the distortion of $\mathbf{N}(\mathbf{r})$. In contrast, for a particle with $n_{\text{p}} > n_{\text{e}} > n_{\text{o}}$, there is only one stable trapping point, that within the particle, although it is not necessarily located at its center (as commonly observed for colloidal spheres in isotropic fluids). The number and positions of the trapping points thus depend on the relative refractive index of the particle as well as the shape of the RIC it generates around itself. A particle with quadrupolar RIC can be trapped at its center, or at two high-n_{eff} points in the RIC or even at four different points in the RIC, depending on the value of n_{p} as well as the laser trap's polarizations (see figure 2 for the shapes and polarization-dependent refractive index patterns of the RICs).

At trapping laser powers above the so-called Freedericksz transition (an optical analog of the electric-field-induced realignment of $\mathbf{N}(\mathbf{r})$ commonly utilized in LC information displays), the trap produces elastic distortion in the LC. Thus, trapping assisted by the optical gradient forces is accompanied by elastic interaction of the particle with the optically distorted region of LC to minimize the elastic energy given by equation (1) [46, 47, 49]. Therefore, optical trapping and manipulation in this case are determined not only by the typical combination of optical gradient and scattering forces but also by the elastic forces between the laser-induced elastic distortion and that due to the colloidal inclusion. We give a more detailed account of properties of optical trapping in this regime in section 6.

3.3. Multistable trapping and particle dynamics in LCs

Particle dynamics in LC media differs from that in isotropic ones. This is due to the anisotropy of both visco-elastic and optical trapping properties in LCs [49]. Even when no laser traps are present, video-microscopy of the Brownian motion of the particle reveals the anisotropic angular patterns of the particle's displacement, showing that the mean displacement along and perpendicular to $\mathbf{N}_0$ are different, see figure 5(a). When such a particle is trapped, the anisotropic pattern of displacements changes upon varying the laser power. The

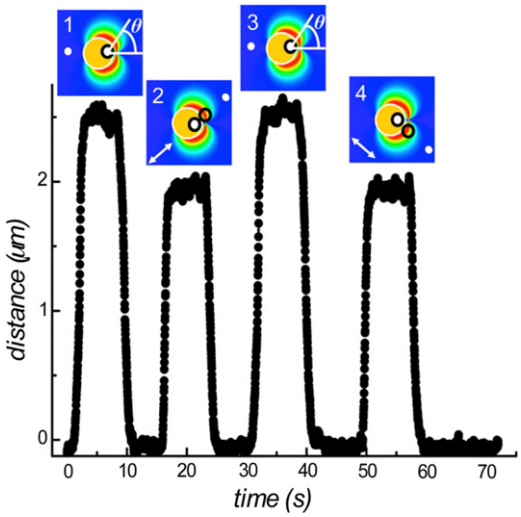

Figure 4. Trapping of colloidal particles with dipolar $\mathbf{N}(\mathbf{r})$. Distance of the particle from the initial position of the trap (filled white circle with a black circumference) versus time as the position of the trap is instantaneously switched to a different point (marked by a filled white circle) and back. Cases 1 and 3 correspond to motion along the dipolar axis. In cases 2 and 4, the equilibrium trap position is marked by a hollow black circle and it lies outside the particle, depending on the direction of motion of the particle (shown by the white double arrows). The results of this experiment demonstrate that three stable or metastable trapping sites (marked by the open black circles) are possible for such particles with RICs; this is in contrast to the case of colloidal spheres in isotropic fluids for which the center of the spherical particle lies directly on the optical axis of the trapping beam, slightly shifted downstream with respect to the center of the trap's focus. The color scale is the same as in figure 3. See [49] for details. (Color online.)

forces experienced by the particles include the random thermal fluctuational force, the viscous drag and the trapping force. We neglect the inertial forces, owing to low velocities (v) of the particles and high viscosity (η) of the media under consideration, i.e. in the low Reynolds number regime. The forces acting on the particle are: $F_{\text{thermal}} = F_{\text{drag}} + F_{\text{trap}}$. For a particle with radius R, F_{drag} is $F_{\text{drag}(\parallel/\perp)} = 6\pi\eta_{(\parallel/\perp)}Rv$ (here the subscripts represent the direction parallel ($\parallel$) or perpendicular ($\perp$) to $\mathbf{N}_0$). Since $\eta_{\parallel} < \eta_{\perp}$ for nematic LCs, it follows that $F_{\text{drag}\parallel} < F_{\text{drag}\perp}$. In contrast, F_{trap} depends on the trap stiffness which is direction-dependent and depends on the particular RIC formed around the colloid. It behaves in a Hookean manner for small distances from the trap center ($r < R$): $F_{\text{trap}(\parallel/\perp)} = \alpha_{(\parallel/\perp)}r$, where r is the distance between the particle and the center of the trap. For particles with the dipolar $\mathbf{N}(\mathbf{r})$, one observes $\alpha_{\parallel} > \alpha_{\perp}$ and, consequently, $F_{\text{trap}\parallel} > F_{\text{trap}\perp}$. This leads to an interesting behavior of the particle dynamics as a function of laser power shown in figure 5(b). At lower trapping powers, the displacement along $\mathbf{N}_0$ is larger than that perpendicular to $\mathbf{N}_0$ (due to the lower viscosity along $\mathbf{N}_0$ and negligible influence of the trapping force anisotropy). However, this behavior reverses for higher laser powers at which the trapping forces become stronger than viscous forces. From the optical trapping standpoint, the LC spherical colloid with the RIC around it effectively behaves as a particle with an anisometric shape with different effective sizes along and

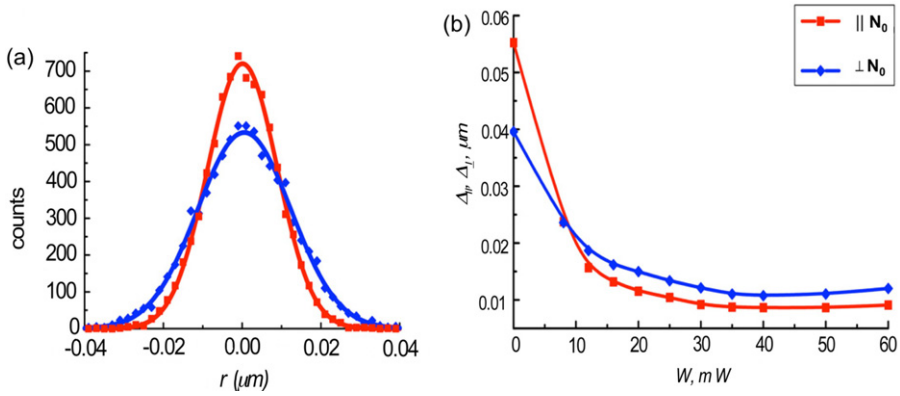

Figure 5. Dynamics of optically trapped colloids. (a) Brownian displacement histograms showing the anisotropy between displacements along the directions parallel (squares) and perpendicular (diamonds) to $\mathbf{N}_0$. (b) The widths of displacement distributions along and perpendicular to $\mathbf{N}_0$, $\Delta_\parallel$ and $\Delta_\perp$ versus the laser trapping power, W. For further reference, see [49].

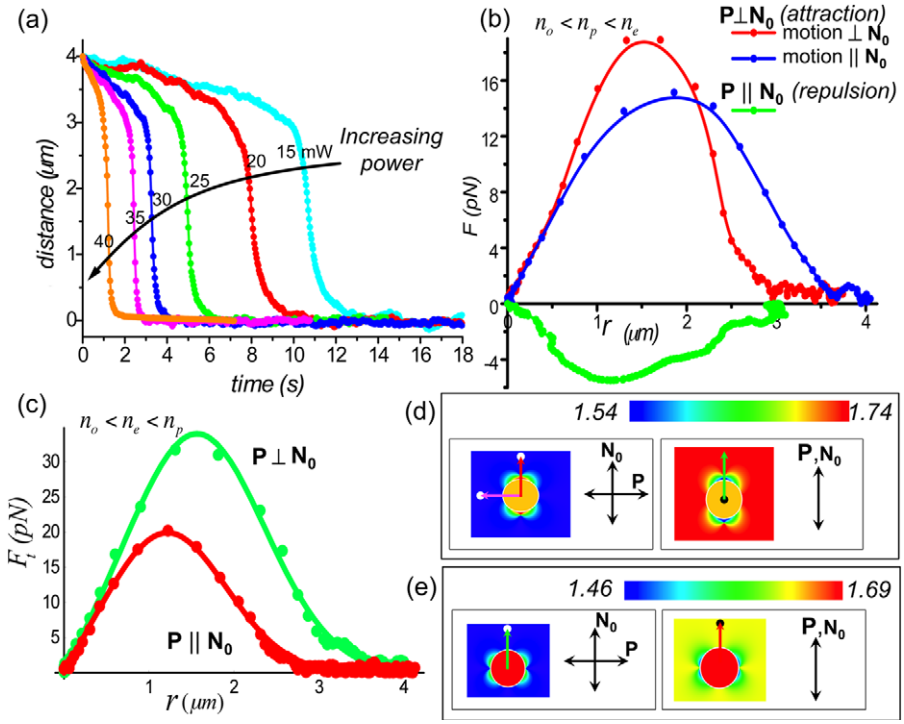

Figure 6. Anisotropy and polarization dependence of optical trapping forces. (a) Distance of a quadrupolar particle from the center of the trapping beam, as the particle falls into the trap; values of the corresponding trapping laser power are marked next to the respective curves. These data are used to obtain force versus distance dependences similar to the ones shown in (b) and (c). (b) Polarization-dependent anisotropy of optical trapping force: (1) for $\mathbf{P} \parallel \mathbf{N}_0$ (repulsive force—green curve online); (2) for $\mathbf{P} \perp \mathbf{N}_0$ (attractive trapping potential—blue and red curves online) and for trapping directions along (blue online) and perpendicular (red online) to $\mathbf{N}_0$ for a particle with refractive index intermediate between n_o and n_e. (c) For a quadrupolar particle having refractive index higher than both n_e and n_o, trapping is polarization-dependent but the particle is attracted to the laser trap for all polarizations. (d) Schematic of the experiment used to deduce the force versus distance dependences shown in (b) along with the corresponding refractive index patterns and the color-coded index scale: for $\mathbf{P} \perp \mathbf{N}_0$, by tracking the particle motion from its original position to the laser trap locations marked by white circles, one obtains the trap–particle distance versus time data similar to that shown in (a) and then the force versus distance curves in part (b); for $\mathbf{P} \parallel \mathbf{N}_0$, the particle moves away from the laser beam initially at its center (marked by the black filled circle on the right-side schematic). (e) Schematic representation of the experiment used to obtain the force–distance relation shown in (c): the particle is set moving to a laser trap for polarizations $\mathbf{P} \perp \mathbf{N}_0$ (white filled circle) and $\mathbf{P} \parallel \mathbf{N}_0$ (black filled circle) and the resulting particle–trap distance versus time dependences are used to obtain the red and green force versus distance curves shown in (c). The reader is directed to [49] for details. (Color online.)

perpendicular to $\mathbf{N}_0$. In the case of a colloid with dipolar $\mathbf{N}(\mathbf{r})$, the effective size of the RIC perpendicular to $\mathbf{N}_0$ is larger than that along $\mathbf{N}_0$, see figures 2(d)–(f). Hence, the effect of the trap is felt further along the direction perpendicular to $\mathbf{N}_0$ and the trap stiffness is lower along that direction, explaining the anisotropic particle dynamics at high laser powers, see figure 5(b).

Figure 6 shows how anisotropic optical trapping features manifest themselves in the case of similar colloids with quadrupolar $\mathbf{N}(\mathbf{r})$ when immersed in two different nematic

LCs. The value of n_p is between that of n_o and n_e in the nematic 5CB while n_p is higher than both n_o and n_e in the AMLC-0010 mixture (see table 1 for its material properties). The trapping force as a function of distance between the particle and the trap focus can be measured by tracking the motion of a particle falling into an optical trap, as schematically shown in figure 6(d). For calculation of the viscous forces, it is reasonable to assume a low Reynolds number regime (viscous forces are significantly greater than inertial forces) and also a low Ericksen number regime (i.e. assuming that the flow does not modify $\mathbf{N}(\mathbf{r})$ around the colloid). Therefore, the trapping force at each point equals the viscous drag force and the Stokes law can be used to compute the viscous force acting on the particle, $F_{drag} = 6\pi\eta Rv$, where η is the effective viscosity. The meaning of the 'radius' R of the particle can rightfully be brought into question, as the effective radius of the particle with a corona around it is larger than the actual radius of the solid sphere. The viscosity η is a complex combination of various viscosity coefficients of the anisotropic LC medium (see [49] for more details). The particle trajectories obtained for various values of trapping power, figure 6(a), can be analyzed to reconstruct the trapping force versus distance relations. The force–distance plot thus obtained looks qualitatively similar to what one would observe in the case of isotropic media. The anisotropy is apparent upon comparing the trapping forces for particle movement along and perpendicular to $\mathbf{N}_0$ as well as in the positions of the maxima in the two cases, see figures 6(b) and (c). For $n_o < n_p < n_e$ (e.g. melamine resin beads in 5CB), a laser trap with polarization $\mathbf{P} \perp \mathbf{N}_0$ is attractive and has direction-dependent trapping forces and stiffness. However, for the polarization $\mathbf{P} \parallel \mathbf{N}_0$, the same laser beam exerts a repulsive optical gradient force, see figures 6(b) and (d). On the other hand, for an LC–particle combination such that $n_o < n_e < n_p$, the trap is attractive regardless of the polarization state of the trapping beam; however, the trap stiffness and the maximum 'escape' forces depend on the laser polarization, see figures 6(c) and (e) [49]. Figures 3–6 show that optical trapping of colloidal particles in anisotropic fluids exhibits features of strong polarization sensitivity and anisotropy that are not encountered in the conventional isotropic host media [49].

3.4. An example of practical application: colloidal interactions in LCs

Colloidal dispersions of particles in LCs (also known as 'liquid crystal colloids') are fascinating soft matter systems from both fundamental and technological points of view [41, 42, 47, 48, 54]. About a dozen years ago Poulin *et al* demonstrated that colloidal particles embedded in the LC solvent can be stabilized by particle-induced topological defects and interact via a new type of interaction that arises from orientational elasticity of the anisotropic host [41]. Thereafter, a broad range of self-assembled colloidal architectures have been reported in the bulk and at the surfaces of LCs [48], promising a new class of self-assembled reconfigurable composites that may soon enable mass production of tunable optical metamaterials and photonic crystals. Particles in the LC host introduce long-range elastic deformations and spatial gradients in $\mathbf{N}(\mathbf{r})$ [41]. Elastic deformations usually have dipolar or quadrupolar symmetry and the ensuing elastic energy strongly depends on the particles' relative positions, giving rise to anisotropic interactions mediated by the LC's elasticity. These interactions are reminiscent of electrostatic interactions exhibited by dipolar charge distributions. Thus, LCs can provide conceptually new physical means of pre-designed control over self-organization of micrometer-and nanometer-sized particles that are not accessible in isotropic hosts. Hence it is important to quantitatively characterize and conceptually understand these elastic colloidal interactions in LCs.

To demonstrate how the laser tweezers provide the capability of characterization of anisotropic elasticity-mediated forces in the LC, we utilize particles surface-treated for tangential boundary conditions that give rise to quadrupolar director structures around them when immersed in a nematic LC. Figures 7(a) and (b) show a map of their orientation-dependent interactions obtained by holding one particle trapped and releasing the other particle at different locations in the sample. By video tracking the particle motion under the action of elasticity-mediated interparticle forces and due to thermal fluctuations, one can decipher both amplitude and direction of the pair-interaction forces. Each time the original distance between the two is kept the same while the interparticle separation angle with respect to $\mathbf{N}_0$ is varied to obtain the plot shown. The separation is large enough that the second particle does not feel the short-range trapping force and only the longer-range quadrupolar interactions are monitored. The force-vector profile obtained for such a colloidal pair of elastic quadrupoles is shown in figure 7(b). One can also measure the distance dependence of the interaction forces directly using optical tweezers in a quasi-static process [48]. Two particles can be trapped and set up at any desired initial positions relative to each other. Trapping power at one of the particles is reduced until it is just released from the trap; the trapping force at that power equals the interaction force between the particles. From such experiments, one finds that the force follows the $1/r^6$ dependence for interparticle separation greater than $\sim 1.5D$ (D is the diameter of the particle), see figure 7(c), which is the same power law dependence as that observed for electric quadrupoles.

Particles with surface treatment such that they have normal boundary conditions for LC molecules at their surfaces form elastic dipoles (although they can also form a quadrupole under certain conditions, as explained in section 3.1), with a virtual point defect of topological charge $+1$ at their center and the hyperbolic hedgehog point defect next to the particle (topological charge -1), see figures 2(d)–(f). The theory of interaction between two such particles was developed by Lubensky *et al* [43]; its results are confirmed by laser trapping experiments, see figure 7(d). For particles with their elastic dipoles oriented in parallel fashion, there is an attractive force along the axis of the dipole, see the inset of figure 7(d). The far-field elastic force between two such particles follows the $1/r^4$ distance dependence (resembling that of electrostatic dipoles), as shown in figure 7(d) [44, 48]. Thus, a complete map

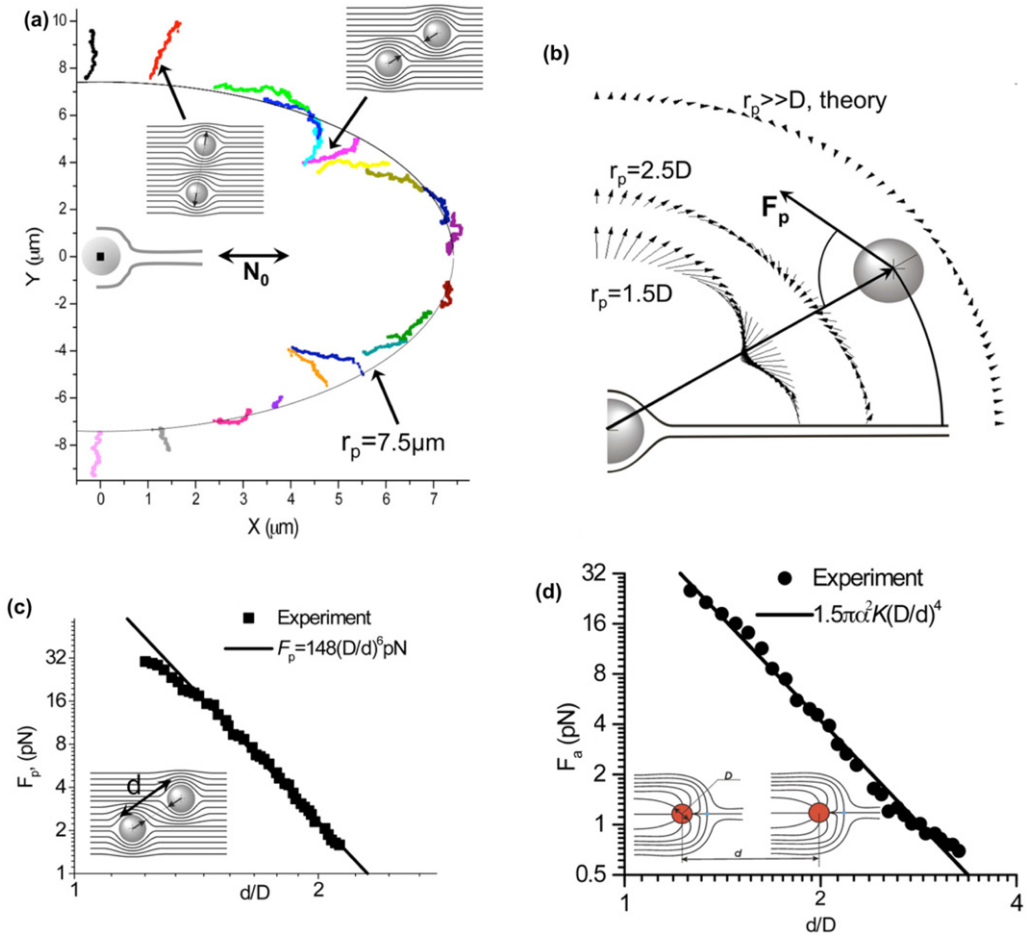

Figure 7. Quantitative characterization of quadrupolar and dipolar colloidal interactions in LCs. (a) Direct probing of the angular dependence of interaction between two quadrupolar particles (3 μm diameter) separated by the initial distance of 7.5 μm: one particle is held trapped at the position $x = y = 0$ while the other is released at different locations so that the inter-particle separation vector makes different angles with respect to $\mathbf{N}_0$; the motion trajectories obtained for different initial locations of the particles are shown using different colors. The two insets show schematic $\mathbf{N}(\mathbf{r})$ and force directions for the cases of attractive and repulsive interactions. (b) Orientation dependences of the force vector for different interparticle separations. (c) Experimental dependence of the attractive force on distance for $\theta = 30^\circ$ compared with the theoretical prediction. The inset shows the initial particle positions and respective $\mathbf{N}(\mathbf{r})$. (d) The distance dependence of the force of attraction between two particles of diameter 3 μm with dipolar $\mathbf{N}(\mathbf{r})$ and parallel dipole moments positioned as shown in the inset. For more details, the reader is directed to [48, 53].

of anisotropic elasticity-mediated pair-interaction forces and their dependence on distance can be determined using laser tweezers. For more details on characterization of interparticle forces in LCs, the reader is referred to [44, 48, 53].

4. Manipulation of self-organized director structures and defects

4.1. Structures and defects in LCs: an introduction

Defects in ordered condensed matter media are important for multiple fundamental and applied reasons [90], such as the study of defect-mediated phase transitions, modeling of defects in cosmology, formation of physical gels, etc. For example, LCs can be used as a test-bed for studying the so-called 'cosmological Kibble mechanism' of defect dynamics in the early universe [91–94]. Furthermore, mechanical properties (for example, plasticity of metals) of ordered media are strongly governed by the presence of defects therein. In the case of LCs, the presence of defects affects the optical characteristics and is often not desirable in displays and other electro-optic devices based on LC technology.

The defects in nematic and cholesteric LCs are the sites—points, lines or walls—on which the orientational order breaks down and $\mathbf{N}(\mathbf{r})$ cannot be defined. The line defects, called 'disclinations', are characterized by their strength (m), which is defined as the number of revolutions by 2π that the director makes while one circumnavigates the core of the defect line once. Typically, the half-integer nematic defect lines are stable while the integer-strength line defects transform into structures with non-singular cores by 'escaping into the third dimension' [1]. Although occasionally defects can be manipulated using electric and magnetic fields [95, 96], this manipulation opens only a narrow range of possibilities for their quantitative study. Owing to elastic constants of LCs (typically in the range of several pN, see table 1), the defects

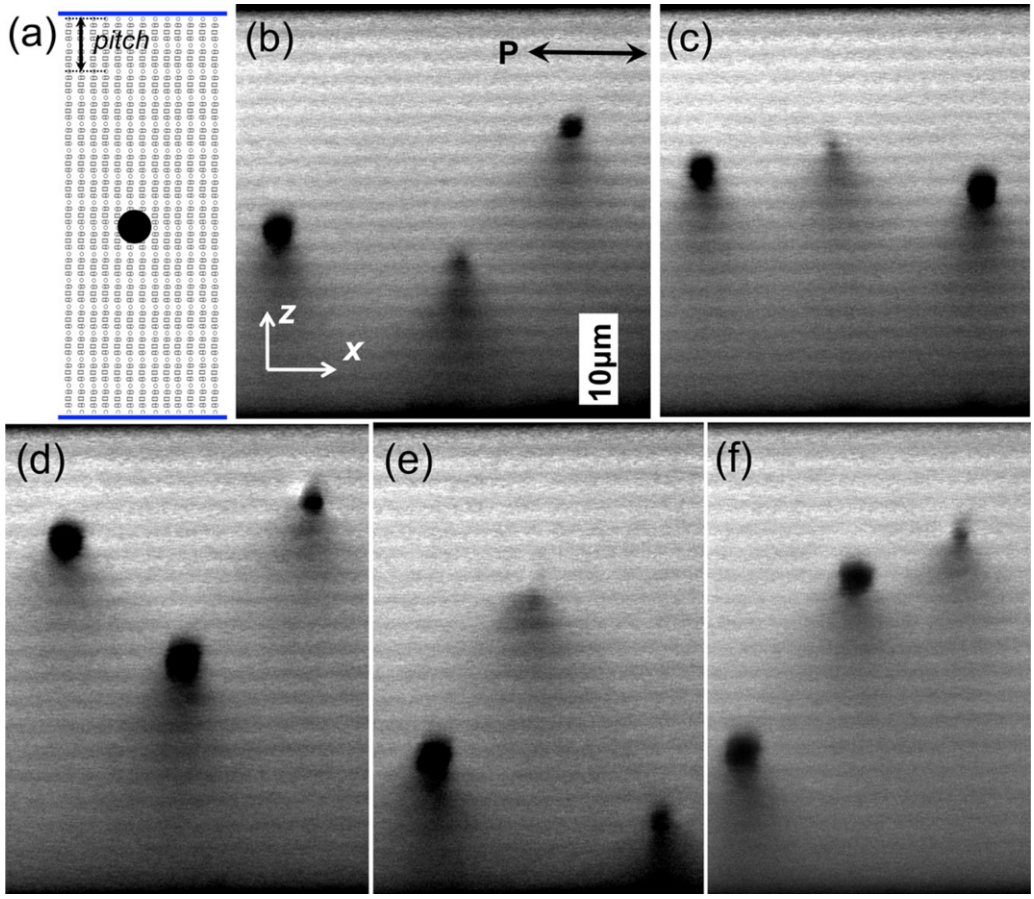

Figure 8. 3D particle manipulation in a cholesteric LC. (a) Schematic representation of the cholesteric LC confined between two substrates with planar anchoring, in presence of a colloidal inclusion (black filled circle). (b)–(f) Vertical cross-sectional images taken using FCPM showing three melamine resin spherical particles which are moved across the layers of the cholesteric LC cell by use of the holographic optical tweezers.

in LCs are aptly suited for manipulation and characterization with optical tweezers. To demonstrate this, below we provide several examples of successful optical manipulation and quantitative characterization of defects in nematic and cholesteric LCs.

4.2. Manipulation of colloidal particles in periodically twisted cholesteric liquid crystals

Molecular chirality gives rise to many interesting chiral condensed matter phases [1, 2]. In the cholesteric phase of chiral nematic LCs, molecules twist uniformly along the axis of a helix; the corresponding ground-state configuration is schematically shown in figure 8(a). The FCPM cross section of a cholesteric cell with a planar surface anchoring at the confining substrates shows a layered pattern as seen in figures 8(b)–(f). Cholesteric LCs can have layer spacings ranging from a few hundred nanometers to hundreds of microns, which is convenient for direct visualization of structures around inclusions and defects using optical microscopy. Therefore, chiral nematics are useful model systems for the study of condensed matter defects and we will show how they have been used to illustrate the capabilities of non-contact optical control of 3D structures and defects with optical tweezers.

Before proceeding to manipulation of cholesteric defects by using colloids as 'handles', we show simultaneous 3D optical manipulation of three melamine resin particles (4 μm in diameter) in a uniformly twisted cholesteric LC confined between substrates with a strong planar surface anchoring, see figures 8(b)–(f). Using holographic optical tweezers (figure 1), the particles are moved both along and perpendicular to the optical axis of the microscope (in the planes of confocal cross sections and perpendicular to them); the configurations after each intermediate step of manipulation are imaged in the vertical cross section using the FCPM (figure 8). Although the forces required to move particles across the cholesteric lamellae are significantly higher than the forces needed to move the same particle within a cholesteric 'layer' [82], non-contact 3D optical manipulation in cholesterics is clearly possible.

4.3. Quantitative characterization of defects: an example of line tension measurement for a nematic disclination

Particle-assisted or direct non-contact optical manipulation of defects in nematic LCs can reveal their topological properties

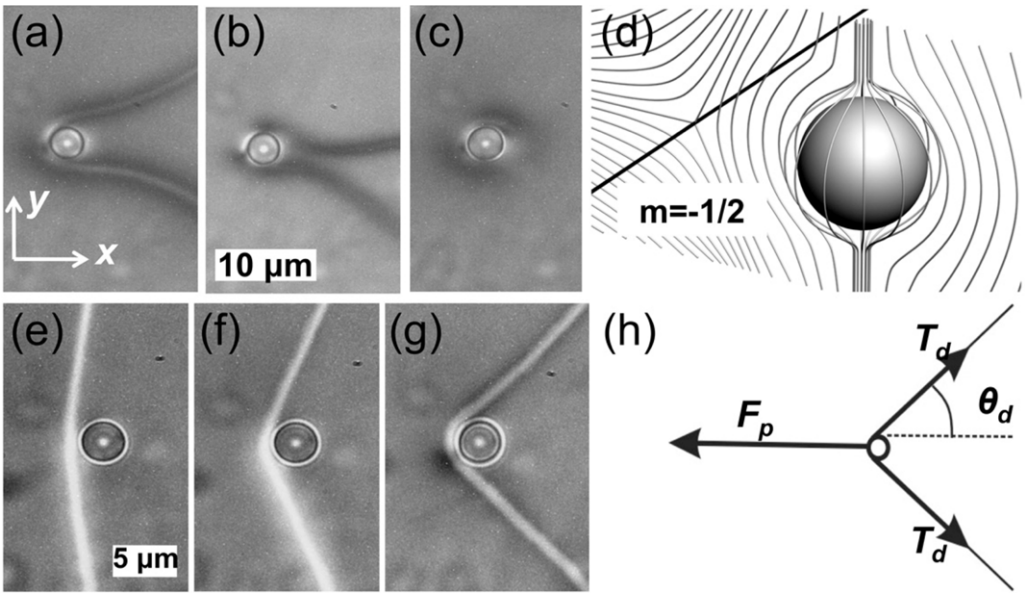

Figure 9. Particle-assisted defect manipulation and measurement of their line tension in a nematic LC. (a)–(c) Manipulation of a disclination of half-integer strength ($m = -1/2$) using a particle with tangential surface anchoring. The particle adheres to the defect line as it is brought closer and pushed along the direction transverse to the disclination length. Eventually, the particle and the defect separate (c), with the defect line straightening to minimize its total energy. (d) Schematic representation of a particle with tangential anchoring and two boojum defects adjacent to an $m = -1/2$ disclination; note that the initial positions of the boojums ((a), (d)) are along the vertical direction and that (c) they reside in the horizontal equatorial plane after the laser-induced manipulation and when the particle is located in the part of the sample with in-plane $\mathbf{N}(\mathbf{r})$. ((e)–(g)) A particle with tangential surface anchoring used to manipulate a disclination of strength $m = +1/2$. In this case, the tangential anchoring does not favor the particle sticking to the defect line, and hence the defect line can be bent and stretched in its transverse direction. (h) Schematics showing how the particle-assisted defect manipulation and calibrated trapping force F_p are used to measure the defect's line tension T_d. For further details on defect manipulation in nematics, see [53, 55].

and line tension (free energy per unit length) [53, 55, 56]. For example, figure 9 shows different types of particle-assisted manipulation conducted on half-integer disclinations of opposite signs. Figures 9(a)–(c) show the $m = -1/2$ disclination manipulated with a melamine resin polymer bead of 4 μm in diameter. The director pattern $\mathbf{N}(\mathbf{r})$ due to the tangential surface anchoring at the particle–LC interface close to the disclination is shown in figure 9(d). This disclination has a singular defect core of size comparable to the size of a molecule (a few nanometers for a thermotropic nematic LC) and tends to pin to the particle's surface. Upon manipulation, the stretched disclination and the bead eventually separate and the disclination shrinks to reduce free energy proportional to its length. Figures 9(e)–(h) show a different kind of particle-assisted manipulation of a half-integer $m = +1/2$ disclination. In this case, the tangential anchoring on the particle surface is not compatible with the director structure around the disclination. Therefore, the defect line is repelled from the approaching colloid and one can use an optically trapped particle to push the disclination along the transverse direction of its length and thus measure the line tension thereof. From the force balance and using the calibrated force of the trap, one can estimate the defect line tension for the $m = +1/2$ disclination, which for the disclination shown in figures 9(e)–(g) is found to be $\sim$75 pN, in agreement with the theoretical predictions [53, 55]. Manipulation of nematic defects is discussed in detail in [53, 55, 56].

4.4. Probing defect topology: an example of defects in cholesteric LCs

Owing to the typical values of the thickness of the cholesteric lamellae, the defect structures in cholesteric LCs can be optically imaged as well as controlled and manipulated. The most common elementary topological defects in translational order of the cholesteric 'layers' are dislocations and the so-called oily streaks, which can have their cores split into various disclinations (the reader is directed to [90, 97] for a detailed account of the classification of cholesteric defects). Figure 10 depicts optical manipulation of an 'elementary oily streak' which is composed of dislocations having Burgers vectors with opposite direction, and has the net Burgers vector equal to zero. An elementary oily streak (also called a 'Lehmann cluster') consists of a quadrupolar assembly of the so-called non-singular λ disclinations (two $\lambda^{+1/2}$ and two $\lambda^{-1/2}$). The corresponding FCPM cross-sectional image and a schematic molecular director structure are shown in figures 10(d) and (h). Similar to the case of defect lines in nematic LCs, particle-assisted manipulation of these cholesteric defects is also possible; colloidal particles can be trapped and pushed in the direction orthogonal to the cluster, see figures 10(a)–(c). Calibrated trapping forces can then be used in the measurement of line tension of clusters [56]. Figures 10(e)–(g) shows planar and cross-sectional images of two particles being used to manipulate a cluster of disclinations perpendicular to the cholesteric layers; this kind of manipulation of the Lehman cluster defects is energetically costly and difficult when using

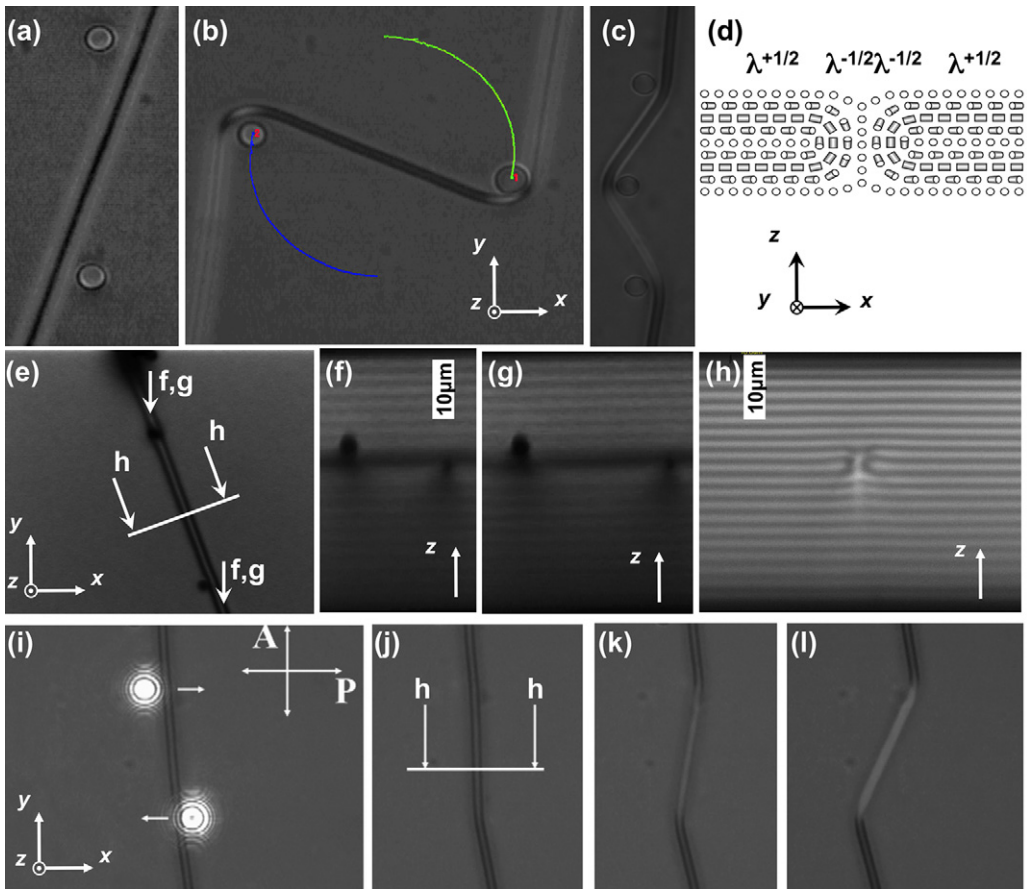

Figure 10. Optical manipulation of disclination clusters in a cholesteric LC. (a)–(c) Particle-assisted manipulation of a Lehman cluster in the xy plane. The particles pushed orthogonally to the length of the disclination cluster induce tension by stretching it; the defect eventually relaxes by straightening itself upon releasing the traps in the absence of trapping forces acting on the colloidal particles to balance the line tension of the defect. (d) Reconstructed molecular structure of a Lehman cluster consisting of four non-singular λ disclinations. (e) Planar FCPM image of two particles used to manipulate a Lehman cluster in the vertical direction. ((f), (g)) Vertical FCPM cross sections along the length of a cluster between end-points for part (f) marked by the arrows labeled 'f' in part (e); it is energetically more difficult to move a cluster across the layers of cholesteric LCs as compared to moving it within the same layer. (h) Vertical cross-sectional image of a Lehman cluster along the plane marked in ((e), (j)) obtained using FCPM. ((i)–(l)) Direct manipulation of a cholesteric Lehman cluster using a laser trap having linear polarization parallel to the cluster; the localized non-uniform director structure of the cluster shown in (d) provides refractive index contrast (for the laser polarization used, the defect core has index $\approx n_e$, higher than that of the LC away from the defect), enabling the direct optical manipulation thereof. For further details on defect manipulation in cholesterics, the reader is referred to [56].

axial trapping forces obtained by optical tweezers at laser powers below the optical realignment threshold. It is to be expected that the motion of a cluster is much more difficult across the lamellae (the so-called 'glide' motion) than that within the same lamellae ('climb' of a defect line) [97].

Molecular structure of a Lehmann cluster, figure 10(h), is such that $\mathbf{N}(\mathbf{r})$ in its center is aligned along the length of the cluster and hence a beam of light polarized along this direction 'sees' the local refractive index close to n_e, higher than that of the surrounding medium, enabling direct optical manipulation of the disclination cluster using optical gradient forces exerted by laser traps. A beam polarized orthogonal to the line but having sufficiently high power (typically greater than 40–50 mW, depending on the optical and elastic properties of the LC) can reorient $\mathbf{N}(\mathbf{r})$ locally, forcing it to be along the polarization of the beam (similar to the effect known as the optical Freederickz transition). This subsequently changes the optical trapping properties, as then $\mathbf{N}(\mathbf{r})$ is locally aligned along the linear polarization direction, and therefore the effective refractive index seen by the beam is $\approx n_e$ (higher than that of the surrounding LC material).

A multitude of factors can lead to the richness in director fields and hence refractive index patterns; these include the surface anchoring at the substrates (planar or homeotropic, strong or weak, etc), presence of inclusions with different anchoring and hence their $\mathbf{N}(\mathbf{r})$ field around them, introduction of chirality and the resultant twisted configurations of a certain equilibrium pitch, the cell thickness, temperature, etc [56]. Figure 11 shows examples of typical $\mathbf{N}(\mathbf{r})$ patterns in cholesteric cells, such as the twisted and untwisted domains in a wedge-shaped cell, see figure 11(a). The domain on the left of figure 11(a) has a uniform $\mathbf{N}(\mathbf{r})$—the surface anchoring forces the LC to be uniform against its inherent tendency to twist while satisfying the strong boundary conditions on the cell substrates. The two domains are separated by a disclination in $\mathbf{N}(\mathbf{r})$ shown in the schematic vertical cross section, see

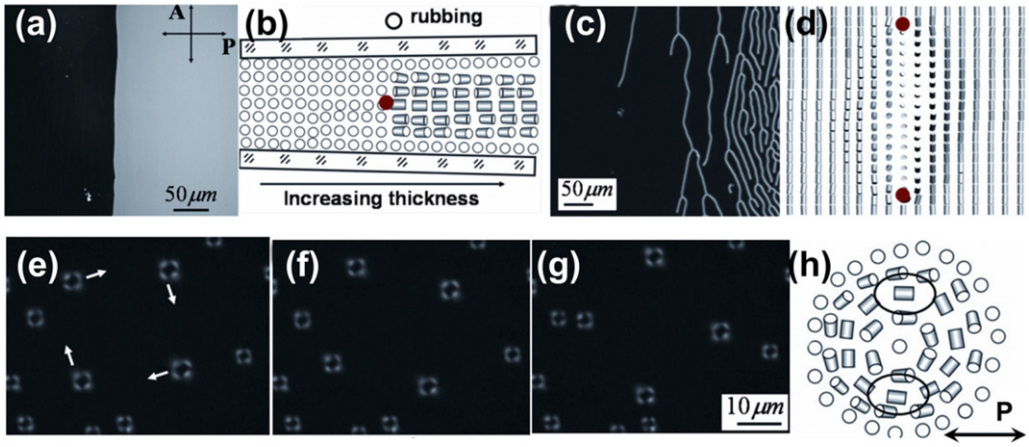

Figure 11. Manipulation of defect structures in a cholesteric LC confined into different cell geometries. (a) Polarizing microscopy image of a sample containing a uniform domain (in the thin part of a cholesteric LC cell, on the left) and 180°-twisted domain, on the right. (b) **N**(**r**) pattern in the vertical plane corresponding to the texture shown in (a). (c) PM texture of the so-called 'cholesteric fingers' of the third type in a homeotropic cholesteric LC cell [56]. (d) Schematics of the cross-sectional director structure of one type of cholesteric fingers. ((e)–(g)) Optical manipulation of localized twisted structures called 'torons' as they are trapped and programmed to move along a circular arc. (h) Schematics of the in-plane **N**(**r**) of the toron in the horizontal plane in the middle of the sample; the regions enclosed in the ellipses are the laser trapping sites as they have local average director orientation parallel to the marked laser trap's linear polarization **P** and hence refractive index $\approx n_e$, higher than that of the surrounding LC with vertical **N**(**r**) and index $\approx n_o$. For a more detailed discussion on manipulation of structures in cholesterics, the reader is directed to [40, 56, 81].

figure 11(b). This boundary between the two domains can be optically shifted along the direction of increasing/decreasing cell thickness based on the polarization of the trapping beam. For a beam polarized along the disclination (the rubbing direction), the untwisted domain can be shifted further into the region with increasing thickness whereas a beam with perpendicular polarization can be used to extend the twisted domain towards the direction of decreasing thickness. This is because the effective refractive index seen by the beam polarized along the rubbing direction in the untwisted region is n_e while it is intermediate between n_o and n_e (and hence $<n_e$) in the twisted region due to spatial variation in **N**(**r**) in that region. The resulting effect is that the beam with said polarization will attract the domain with higher effective refractive index (the untwisted domain) and repel the twisted domain. An orthogonal polarizations state of the trap gives an opposite effect.

Figure 11(c) shows a polarizing microscopy image of the so-called 'cholesteric fingers', which are formed in a cell with homeotropic anchoring on both substrates and with the pitch approximately equal to the cell thickness. The fingers have a localized twist of **N**(**r**) along the helical axis parallel to the cell substrates (the direction of twist being orthogonal to the length of the finger). The homeotropic surface anchoring conditions are met by disclinations close to each substrate. Figure 11(d) shows the director structure in the plane perpendicular to the length of the finger. These fingers can be manipulated using a laser beam with polarization along its axis. Displacing the beam perpendicular to the axis of the finger laterally shifts or stretches the finger. Moving the beam along the length of the finger and past its tip makes it drift along that direction.

Axially symmetric twisted structures called 'torons' can be optically generated or they can spontaneously occur in homeotropic cholesteric cells of thickness approximately equal to the equilibrium CNLC pitch [81]. The detailed description of the internal **N**(**r**) of a toron is outside the scope of the present review and the reader is directed to [81] for references. Figures 11(e)–(g) show how individual torons can be optically trapped and manipulated similarly to immersed colloidal particles. The encircled regions of schematically shown **N**(**r**) in the cell mid-plane, see figure 11(h), are the 'high-index' region for the laser light polarized horizontally, see the inset of figure 11(h), and hence the stable trapping points. Similar to particles, the torons can be set to move along the computer-programmed trajectories, even though these are localized particle-like excitations rather than particles. The motion of a toron is accompanied by a sequential change of the **N**(**r**) pattern.

5. Manipulation of anisotropic colloids in anisotropic fluids: examples of colloidal nanorods in nematic and cholesteric fluids

Optical manipulation of anisotropic particles leads to an interesting trapping behavior, even when the surrounding medium is an isotropic fluid. For example, particles made of birefringent material can be rotated while trapped, as a result of the angular momentum transfer from the beam to a birefringent particle such as a liquid crystal droplet [71–76]. A trapping beam can align disc-shaped and rod-shaped particles (including bacteria) parallel to the light propagation direction or parallel to the linear polarization direction [77–80]. In the case of trapping of anisotropic particles in anisotropic fluids, one usually deals with the preferred equilibrium orientation of the particle with respect to $\mathbf{N}_0$ that minimizes the LC's elastic energy due to director distortions produced by the colloidal inclusion [51]. To illustrate some of the interesting features of manipulation of anisotropic colloids in LCs, we will use an

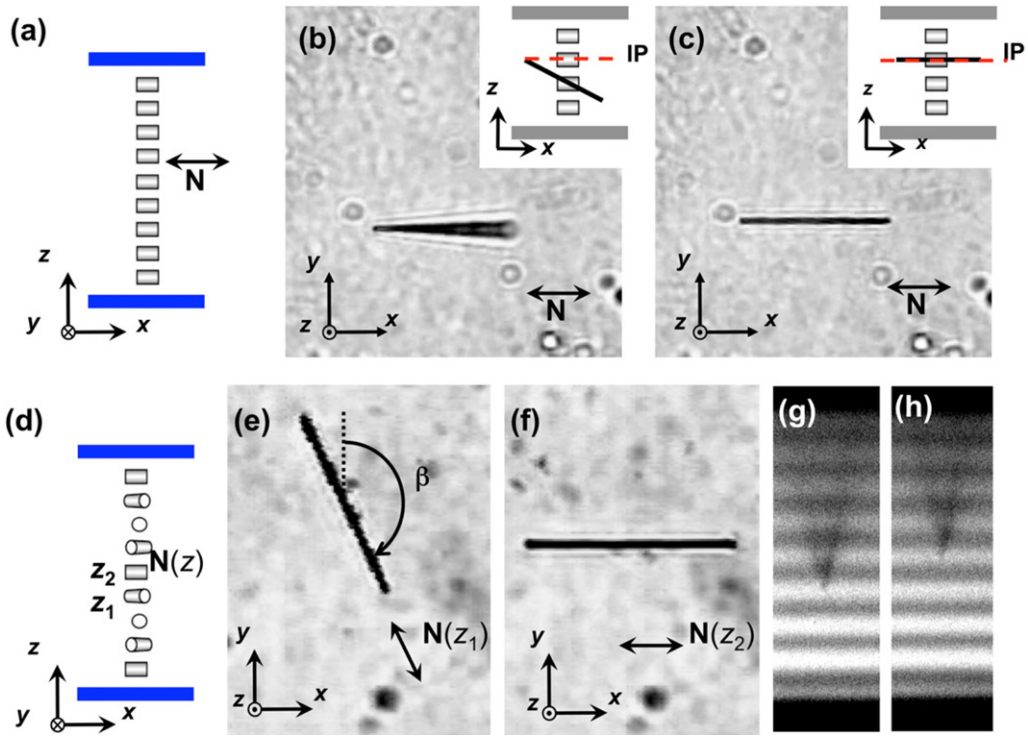

Figure 12. Optical manipulation of nanorods in ((a)–(c)) non-twisted and ((d)–(h)) cholesteric LCs. (a) Schematics of the uniform nematic LC structure in a planar cell. (b) Tilted nanorod that departs from the local orientation of $\mathbf{N}(\mathbf{r})$ due to the action of optical gradient and scattering forces acting on one of its ends; the inset shows the schematics of how the nanorod is aligned in the vertical (x, z) plane (note the actual angle between the nanorod and $\mathbf{N}(\mathbf{r})$ is only several degrees, much smaller than what is shown in the inset for reasons of clarity). (c) Nanorod self-aligned along the local $\mathbf{N}(\mathbf{r})$ (x direction) when no laser trap is used. (d) Schematics of the cholesteric LC structure in a planar LC cell. ((e), (f)) Nanorod aligned along the local director $\mathbf{N}(\mathbf{r})$: the rotation and vertical positions of the nanorod are coupled to each other so that vertical translation of the nanorod from the position at $z = z_1$ to z_2 is accompanied by its rotation for an angle β. ((g), (h)) FCPM vertical cross-sectional images of a cholesteric LC structure before (g) and after (h) a nanorod has been rotated by 180°, showing the movement along the z direction by $p/2$. The position of the nanorod in the FCPM images corresponds to the vertex of the cone-like shadow. The nanowire length in ((b), (c), (e), (f)) is $\approx$10 μm. The thickness of the cholesteric lamella (corresponding to $p/2$) in ((g), (h)) is 2.5 μm. For further details on nanorod manipulation in LCs, see [98].

example of rod-shaped GaN particles with a length of $\sim$10 μm and $\sim$300 nm wide hexagonal cross section utilized to probe director structures and dislocations [98].

When immersed in a nematic LC, the GaN nanorods impose tangential surface boundary conditions for $\mathbf{N}(\mathbf{r})$ and align parallel to $\mathbf{N}_0$ to minimize the elastic free energy, see figure 12(a). A laser trap attracts the rod: however, the rod is also pushed in the direction of the trapping light propagation, see figures 12(b) and (c), making 3D optical trapping in the nematic fluid off-centered with respect to the focal plane of the beam and also often unstable. The reason is the strong scattering force due to the large refractive index mismatch between GaN ($n \sim 2.3$) and the LC ($n \sim 1.5$). Furthermore, in-plane rotation of the rod away from its equilibrium orientation along $\mathbf{N}_0$ is resisted by the LC elasticity; the nanorod can be deviated from $\mathbf{N}_0$ only for small angles of several degrees even when using high-power optical traps, see figure 12(b).

The situation is different when the rods are immersed in a cholesteric LC with a pitch an order of magnitude larger than the rod's lateral size. The rods follow the helicoidal $\mathbf{N}(\mathbf{r})$ structure which also balances the scattering force, preventing the rod from being pushed away from the objective. Thus, stable laser trapping and optical manipulation of GaN nanorods in 3D is possible. However, the chiral nematic liquid crystal (CNLC) structure induces a coupling between position and orientation of each rod: movement along the helicoidal structure is possible only by rod rotation, see figures 12(d)–(h). The CNLC handedness and the rotation direction with respect to it determine whether the rod moves upwards or downwards while following the director $\mathbf{N}(\mathbf{r})$. In contrast, movements within a cholesteric 'layer' require retaining the orientation of the rod. This coupling between rod position and orientation allows such rods to locally probe the director structure and measure the local cholesteric pitch [98]. For instance, to probe the Burgers vector of a dislocation, one can move the rod along the so-called Burgers circuit, see figure 13. Using a combination of in-plane translation and by rotating the rod both clockwise (CW) and counter-clockwise (CCW), the rod circumnavigates the dislocation, figure 13(a), revealing the magnitude of the Burgers vector $b = p/2$ and the defect core structure split into a $\lambda^{+1/2}\tau^{-1/2}$ pair.

Nanorods in cholesterics can be trapped by singular disclination lines within the dislocation cores, see figure 14(a). This occurs to minimize the Frank elastic free energy as a nanorod positioned in the defect core displaces an energetically

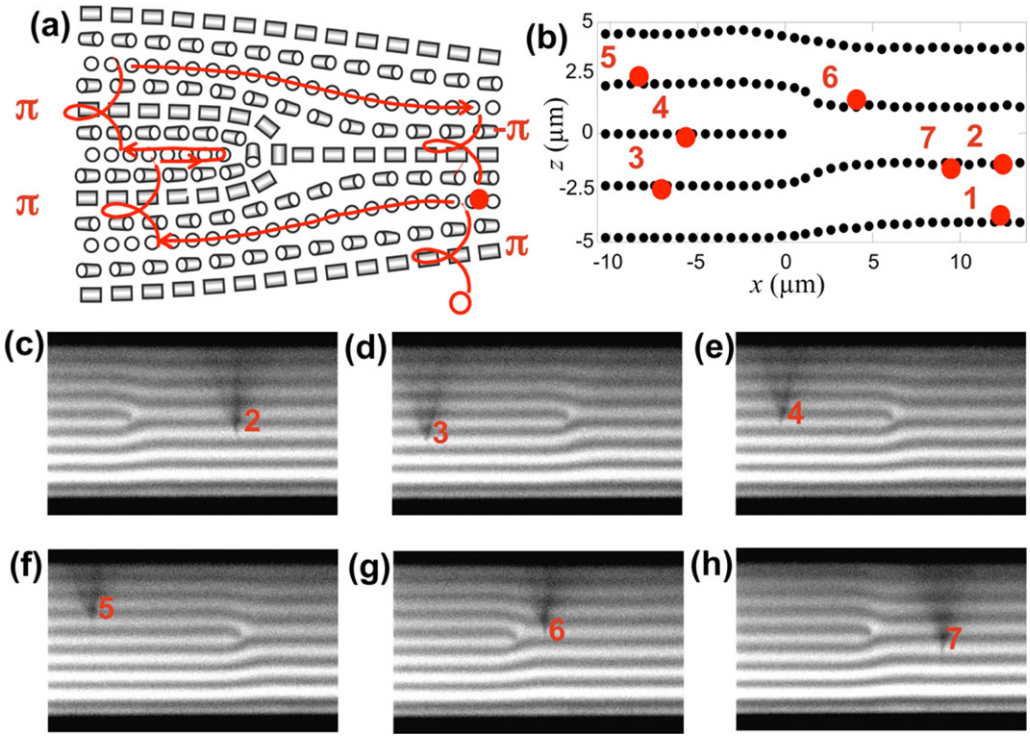

Figure 13. Probing the Burgers vector and internal structure of a dislocation with its core split into a $\lambda^{+1/2}\tau^{-1/2}$ disclination pair. (a) Schematics of the visualized core structure of the $b = p/2$ dislocation; the Burgers circuit and the trajectory (red line) of the nanorod translation used for probing the core of the defect line. Note that the translation of the nanorod between cholesteric layers is accompanied by its rotation. (b) Layer displacement around the edge dislocation; the red filled circles correspond to FCPM images and the measured nanorod positions shown in ((c)–(h)), respectively. ((c)–(h)) FCPM imaging that illustrates direct probing of the Burgers vector by sequential translation of the nanorod along a Burgers circuit that includes points 2–7 marked in the FCPM images ((c)–(h)): (c) Burgers-circuit translation starts at point 2; (d) the nanorod is continuously translated beneath the dislocation to the new location (3) and then (e), rotated by 180° counter-clockwise with the corresponding translational shift upward by one cholesteric layer; moving the nanorod to the right on the image revealed the discontinuity in the layer and the location of the dislocation core; (f) the rod is rotated by 180° counter-clockwise again while shifting one layer upward; (g) the nanorod is moved above the dislocation to position 6 and then (h) rotated by 180° clockwise while shifting one layer downward and closing the Burgers circuit. The equilibrium thickness of the cholesteric lamella corresponding to $p/2$ is about 2.5 μm. For detailed description of defect manipulation with nanorods, see [98].

costly region of the sample. It is easy to translate such a nanorod along the dislocation line using a low-power optical trap. However, it is impossible to separate the rod from the dislocation without using a high optical power above the LC realignment threshold. When the rod is optically manipulated, the defect line closely follows the pinned nanorod, see figures 14(b) and (c). Figures 14(d)–(h) show how a dislocation kink (a transition in height of the dislocation center) is moved using an optically manipulated rod. Even though the images in figures 14(g) and (h) only show a $\sim$10 μm movement, kink translation for distances of at least an order of magnitude longer than the pitch is possible.

6. Optical trapping at laser powers inducing optical realignment of the liquid crystal director

A unique behavior observed in LCs is the optical realignment of $\mathbf{N}(\mathbf{r})$ above a certain threshold optical power, the so-called optical Freederickz transition (briefly mentioned earlier). The value of the threshold optical power depends on the birefringence (Δn) of the material; the higher the value of $\Delta n = n_e - n_o$, the lower the threshold, $W_{th} \sim 1/(n_e^2 - n_o^2)$. Thus the low-birefringence LC materials such as ZLI-2806 (with $\Delta n \approx 0.04$) can be used for laser trapping studies with relatively high values of optical power without worrying about the effects of the optical reorientation influencing the force measurements and defect characterization.

Above the threshold power, the light beam distorts $\mathbf{N}(\mathbf{r})$ locally and thus changes the refractive index pattern which, as a consequence, changes the optical gradient forces. The resultant shape and the effective refractive index can be controlled by the polarization and the power of the beam, giving more ways to tune the trapping properties. Besides, one also observes elasticity-mediated interaction between this locally distorted region of non-uniform $\mathbf{N}(\mathbf{r})$ and the particle/defect structure being trapped; this interaction is of elastic origin, tending to minimize the free energy given by expression (1). Thus, at high powers, non-contact manipulation is mediated by both the gradient forces due to the optically distorted refractive index pattern as well as elastic structural forces. The effect of these elastic forces must be minimized or their contributions accounted for, when trapping is used for quantitative measurements such as the interaction forces between dipolar or quadrupolar colloids or defect line tension.

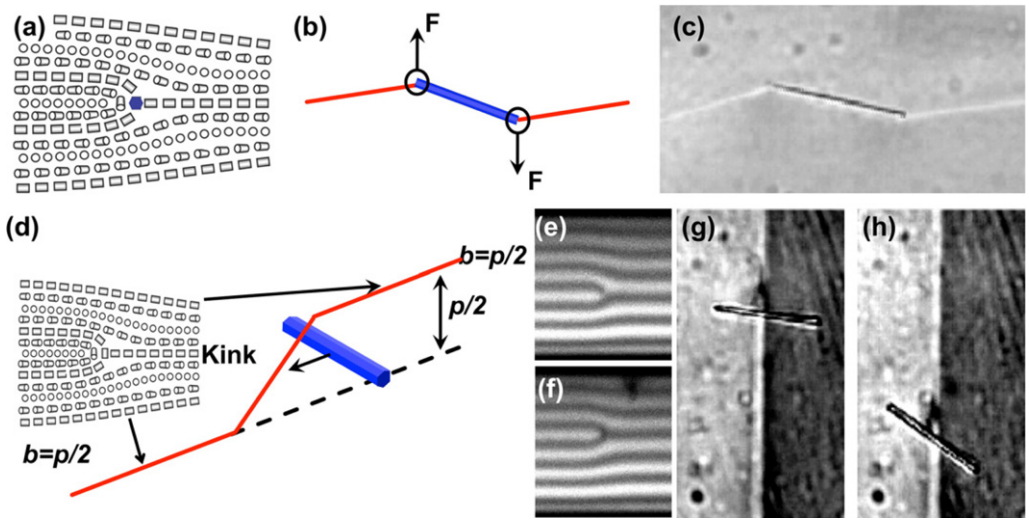

Figure 14. Nanorod-assisted manipulation of cholesteric defects. ((a)–(c)) Optical manipulation of a nanorod localized in a singular τ disclination line. (a) Illustration of the nanorod's position concentric with the τ disclination line. (b) Schematic of the laser-induced manipulation with two traps at the ends allowing manipulation of the nanorod and the defect pinned to it. (c) Optical image of nanorod-assisted manipulation of a disclination line. (d) Illustration of a nanorod positioned next to the dislocation kink. ((e), (f)) FCPM images showing the layer dislocation at different levels in the layered system obtained before and after the kink propagation corresponding to (g) and (h), respectively. ((g), (h)) Optical images showing the edge dislocation with a kink before and after it was pushed for $\sim$10 μm along the length of the defect using the optically manipulated nanorod. The equilibrium thickness of the cholesteric lamella corresponding to $p/2$ is about 2.5 μm. For more details, the reader is directed to [98].

At the same time, this effect allows for manipulation of structures with low refractive index contrast, which are not effectively manipulated at low powers [46]. Even for structures and particles that are otherwise trappable at low laser powers, the local reorientation above the threshold allows for novel ways of manipulating the structure by locally modifying its director field. For more details on realignment-assisted laser manipulation at powers above the threshold, the reader is directed to [46, 47, 49, 53, 56].

7. Conclusion

Optical trapping in anisotropic liquid crystal media is characterized by the polarization dependence of laser trapping forces and can be applied to colloidal particles, defects and structures of long-range molecular order. Manipulation of colloidal inclusions is strongly enriched by polarization dependence of the refractive index of anisotropic fluids and by the presence of refractive index coronas formed around these inclusions due to the boundary conditions for $\mathbf{N}(\mathbf{r})$ set by the treatment of particle surfaces. The polarization-controlled particle motion using a stationary focused laser beam may lead to optically driven microfluidic applications, micro-optomechanical devices, dynamic control and reconfiguration of the assembly of beads into photonic crystals, etc. Optical trapping provides the means for quantitative characterization and understanding of elasticity-mediated colloidal interactions and self-assembly in liquid crystals, and may allow for probing their many-body interactions [41, 99, 100]. The insights provided by optical trapping of particles in LCs benefit a plethora of technological applications of these soft matter systems, namely liquid-crystal-based biosensors [28, 54], self-assembly of metamaterials, and design of colloidal crystals and gels. The ability to probe defects in LCs may provide direct quantitative insights into defect-mediated phase transitions [91–94, 101] as well as helping design solids with tunable elasticity [102], electro-optic materials with controlled optical properties, optical generation of defect structures in LCs to shape laser beams [81, 103], etc.

Acknowledgments

This work was supported by the Renewable and Sustainable Energy Initiative and Innovation Initiative Seed Grant Programs of the University of Colorado at Boulder, the International Institute for Complex Adaptive Matter (ICAM-I2CAM), and by NSF grants DMR-0820579, DMR-0844115, DMR-0645461 and DMR-0847782. DE acknowledges the Swedish Foundation for International Cooperation in Research and Higher Education (STINT) for financial support. We thank Paul Ackerman, Kris Bertness, Noel Clark, Dennis Gardner, Zhiyuan Qi, Taewoo Lee, Yiheng Lin, Angel Martinez, Martin Persson, Leo Radzihovsky, Chuck Rogers, Bohdan Senyuk and Christopher Twombly for discussions.

References

[1] De Gennes P G and Prost J 1995 *The Physics of Liquid Crystals* (New York: Oxford University Press)
[2] Chaikin P M and Lubensky T C 2000 *Principles of Condensed Matter Physics* (Cambridge: Cambridge University Press)
[3] Woltman S J, Jay D G and Crawford G P 2007 *Nat. Mater.* **6** 929–38

[4] Kachynski A V, Kuzmin A N, Prasad P N and Smalyukh I I 2008 *Opt. Express* **16** 10617–32
[5] Camacho-Lopez M, Finkelmann H, Palffy-Muhoray P and Shelley M 2004 *Nat. Mater.* **3** 307–10
[6] De Luca A, Barna V, Atherton T J, Carbone G, Sousa M E and Rosenblatt C 2008 *Nat. Phys.* **4** 869–72
[7] Clark N A and Lagerwall S T 1980 *Appl. Phys. Lett.* **36** 899–991
[8] Yang D K, Doane J W, Yaniv Z and Glasser J 1994 *Appl. Phys. Lett.* **64** 1905–7
[9] Kim J-H, Yoneya M and Yokoyama H 2002 *Nature* **420** 159–62
[10] van Oosten C L, Baastiansen C W M and Broer D J 2009 *Nat. Mater.* **8** 677–82
[11] Yamamoto J and Tanaka H 2005 *Nat. Mater.* **4** 75–80
[12] Liu Q, Cui Y, Gardner D, Li X, He S and Smalyukh I I 2010 *Nano Lett.* **10** 1347
[13] Pratibha R, Park W and Smalyukh I I 2010 *J. Appl. Phys.* **107** 063511
[14] Pratibha R, Park W and Smalyukh I I 2009 *Opt. Express* **17** 19459–69
[15] Caillaud B, Dupont L, Gautier P, de Bougrenet de la Tocnaye J-L, Rudquist P, Engström D, Jägemalm P and Lagerwall S T 2008 *Ferroelectrics* **364** 66–71
[16] Engström D, O'Callaghan M J, Walker C and Handschy M A 2009 *Appl. Opt.* **48** 1721–6
[17] Hällstig E, Öhgren J, Allard L, Sjöqvist L, Engström D, Hård S, Ågren D, Junique S, Wang Q and Noharet B 2005 *Opt. Eng.* **44** 45001
[18] Smalyukh I I, Butler J, Shrout J D, Parsek M R and Wong G C L 2008 *Phys. Rev.* E **78** 030701(R)
[19] Brake J M, Daschner M K, Luk Y Y and Abbott N L 2003 *Science* **302** 2094–7
[20] Smalyukh I I, Zribi O V, Butler J C, Lavrentovich O D and Wong G C L 2006 *Phys. Rev. Lett.* **96** 177801
[21] Hulmes D J 2002 *J. Struct. Biol.* **137** 2–10
[22] Blanc N S, Senn A, Leforestier A, Livolant F and Dubochet J 2001 *J. Struct. Biol.* **134** 76–81
[23] Livolant F 1991 *Physica* A **176** 117–37
[24] Nazzal S, Smalyukh I I, Lavrentovich O D and Khan M A 2002 *Int. J. Pharm.* **235** 247–65
[25] Zribi O, Kyung H, Golestanian R, Liverpool T and Wong G C L 2005 *Europhys. Lett.* **70** 541–7
[26] Vollrath F and Knight D P 2001 *Nature* **410** 541–8
[27] Sivakumar S, Wark K L, Gupta J K, Abbott N L and Caruso F 2009 *Adv. Funct. Mater.* **19** 2260
[28] Gupta V K, Skaife J J, Dubrovsky T B and Abbott N L 1998 *Science* **279** 2077
[29] Schütze K, Pösl H and Lahr G 1998 *Cell. Mol. Biol.* **44** 735–46
Koenig G M, Lin I-H and Abbott N L 2010 *Proc. Natl Acad. Sci. USA* **107** 3998–4003
Smalyukh I I 2010 *Proc. Natl Acad. Sci. USA* **107** 3945–6
[30] Korda P T, Spalding G C and Grier D G 2002 *Phys. Rev.* B **66** 024504
[31] Ashkin A 1997 *Proc. Natl Acad. Sci. USA* **94** 4853–60
[32] Ashkin A 2000 *IEEE J. Sel. Top. Quantum Electron.* **6** 841–56
[33] Grier D G 1997 *Curr. Opin. Colloid Interface Sci.* **2** 264
[34] Jonas A and Zemanek P 2008 *Electrophoresis* **29** 4813–51
[35] McGloin D 2006 *Phil. Trans. R. Soc.* A **364** 3521–37
[36] Curtis J E and Grier D G 2003 *Phys. Rev. Lett.* **90** 133901
[37] Grier D G 2003 *Nature* **424** 810–6
[38] Liesener J, Reicherter M, Haist T and Tiziani H J 2000 *Opt. Commun.* **185** 77–82
[39] Curtis J E, Koss B A and Grier D G 2002 *Opt. Commun.* **207** 169–75
[40] Anand S, Trivedi R P, Stockdale G and Smalyukh I I 2009 *Proc. SPIE* **7232** 723208
[41] Poulin P, Stark H, Lubensky T C and Weitz D A 1997 *Science* **275** 1770–3
[42] Poulin P, Cabuil V and Weitz D A 1997 *Phys. Rev. Lett.* **79** 4862
[43] Lubensky T C, Petty D, Currier N and Stark H 1998 *Phys. Rev.* E **57** 610
[44] Yada M, Yamamoto J and Yokoyama H 2004 *Phys. Rev. Lett.* **92** 18550
[45] Pattanaporkratana A, Park C S, Maclennan J E and Clark N A 2004 *Ferroelectrics* **310** 131–6
[46] Muševič I, Škarabot M, Babič D, Osterman N, Poberaj I, Nazarenko V and Nych A 2004 *Phys. Rev. Lett.* **93** 187801
[47] Škarabot M, Ravnik M, Babič D, Osterman N, Poberaj I, Žumer S, Muševič I, Nych A, Ognysta U and Nazarenko V 2006 *Phys. Rev.* E **73** 021705
[48] Smalyukh I I, Lavrentovich O D, Kuzmin A N, Kachynskii A V and Prasad P N 2005 *Phys. Rev. Lett.* **95** 157801
Smalyukh I I, Chernyshuk S, Lev B I, Nych A B, Ognysta U, Nazarenko V G and Lavrentovich O D 2004 *Phys. Rev. Lett.* **93** 117801
[49] Smalyukh I I, Kachynski A V, Kuzmin A N and Prasad P N 2006 *Proc. Natl Acad. Sci. USA* **103** 18048
[50] Skarabot M, Ravnik M, Zumer S, Tkalec U, Poberaj I, Babic D, Osterman N and Musevic I 2008 *Phys. Rev.* E **77** 031705
[51] Lapointe C, Mason T and Smalyukh I I 2009 *Science* **326** 1083–6
Lapointe C P, Hopkins S, Mason T G and Smalyukh I I 2010 *Phys. Rev. Lett.* **105** 178301
[52] Ivashita Y and Tanaka H 2003 *Phys. Rev. Lett.* **90** 045501
[53] Smalyukh I I, Kuzmin A N, Kachynskii A V, Prasad P N and Lavrentovich O D 2005 *Appl. Phys. Lett.* **86** 021913
[54] Shiyanovskii S V, Schneider T, Smalyukh I I, Ishikawa T, Niehaus G D, Doane K J, Woolverton C J and Lavrentovich O D 2005 *Phys. Rev.* E **71** 020720
[55] Smalyukh I I, Senyuk B I, Shiyanovskii S V, Lavrentovich O D, Kuzmin A N, Kachynski A V and Prasad P N 2006 *Mol. Cryst. Liq. Cryst.* **450** 79
[56] Smalyukh I I, Kaputa D S, Kachynski A V, Kuzmin A N and Prasad P N 2007 *Opt. Express* **15** 4359
Smalyukh I I, Senyuk B I, Palffy-Muhoray P, Lavrentovich O D, Huang H, Gartland E C, Bodnar V H, Kosa T and Taheri B 2005 *Phys. Rev.* E **72** 061707
[57] Hatta E and Fischer T M 2002 *Langmuir* **18** 6201
[58] Wurlitzer S, Steffen P and Fischer T M 2000 *J. Chem. Phys.* **112** 5915
[59] Wurlitzer S, Steffen P, Wurlitzer M, Khattari Z and Fischer T M 2000 *J. Chem. Phys.* **113** 3822
[60] Steffen P, Wurlitzer S and Fischer T M 2001 *J. Phys. Chem.* A **105** 8281
[61] Wurlitzer S, Lautz C, Liley M, Duschl C and Fischer T M 2001 *J. Phys. Chem.* B **105** 182
[62] Hatta E and Fischer T M 2003 *J. Phys. Chem.* B **107** 6406
[63] Wood T A, Gleeson H F, Dickinson M R and Wright A J 2004 *Appl. Phys. Lett.* **84** 4292
[64] Juodkazis S, Shikata M, Takahashi T, Matsuo S and Misawa H 1999 *Appl. Phys. Lett.* **74** 3627
[65] Juodkazis S, Matsuo S, Murazawa N, Hasegawa I and Misawa H 2003 *Appl. Phys. Lett.* **82** 4657
[66] Murazawa N, Juodkazis S and Misawa H 2006 *Eur. Phys. J.* E **20** 435
[67] Murazawa N, Juodkazis S and Misawa H 2006 *Opt. Express* **14** 2481
[68] Murazawa N, Juodkazis S, Jarutis V, Tanamura Y and Misawa H 2006 *Europhys. Lett.* **73** 800

[69] Murazawa N, Juodkazis S, Matsuo S and Misawa H 2005 *Small* **1** 656
[70] Fernández-Nieves A, Cristobal G, Garcés-Chávez V, Spalding G C, Dholakia K and Weitz D A 2005 *Adv. Mater.* **17** 680
[71] Brasselet E and Juodkazis S 2009 *J. Nonlinear Opt. Phys. Mater.* **18** 167–94
[72] Brasselet E, Balčinūas T, Murazawa N, Juodkazis S and Misawa H 2009 *Mol. Cryst. Liq. Cryst.* **512** 143–51
[73] Friese M E J, Nieminen T A, Heckenberg N R and Rubinsztein-Dunlop H 1998 *Nature* **394** 348–50
[74] Friese M E J, Rubinsztein-Dunlop H, Gold J, Hagberg P and Hanstorp D 2001 *Appl. Phys. Lett.* **78** 547
Singer W, Nieminen T A, Gibson U J, Heckenberg N R and Rubinsztein-Dunlop H 2006 *Phys. Rev.* E **73** 021911
[75] Singer W, Rubinsztein-Dunlop H and Gibson U J 2004 *Opt. Express* **12** 6440–5
[76] La Porta A and Wang M D 2004 *Phys. Rev. Lett.* **92** 190801
Deufel C, Forth S, Simmons C R, Dejgosha S and Wang M D 2007 *Nat. Methods* **4** 223
[77] Cheng Z, Chaikin P M and Mason T G 2002 *Phys. Rev. Lett.* **89** 108303
[78] Cheng Z, Chaikin P M and Mason T G 2003 *Phys. Rev.* E **68** 051404
[79] Wilking J N and Mason T G 2008 *Europhys. Lett.* **81** 58005
[80] Gauthier R C, Ashman M and Grover C P 1999 *Appl. Opt.* **38** 4861
[81] Smalyukh I I, Lansac Y, Clark N A and Trivedi R P 2010 *Nat. Mater.* **9** 139–45
Trushkevych O, Ackerman P, Crossland W A and Smalyukh I I 2010 *Appl. Phys. Lett.* **97** 201906
[82] Smalyukh I I and Lavrentovich O D 2002 *Phys. Rev.* E **66** 051703
Smalyukh I I 2007 *Mol. Cryst. Liq. Cryst.* **477** 23–41
[83] Smalyukh I I, Shiyanovskii S V and Lavrentovich O D 2001 *Chem. Phys. Lett.* **336** 88–96
Shiyanovskii S V, Smalyukh I I and Lavrentovich O D 2001 *Liquid Crystals: Computer Simulations, Theory and Experiment* ed O D Lavrentovich, P Pasini, C Zannoni and S Zumer (Dordrecht, The Netherlands: Kluwer Academic) pp 229–70
[84] Kachynski A V, Kuzmin A N, Prasad P N and Smalyukh I I 2007 *Appl. Phys. Lett.* **91** 151905
Lee T, Trivedi R P and Smalyukh I I 2010 *Opt. Lett.* **35** 3447–9
Trivedi R P, Lee T and Smalyukh I I 2010 *Opt. Express* **18** 27658–69
[85] Saar B G, Park H-S, Xie X S and Lavrentovich O D 2007 *Opt. Express* **15** 13585–96
[86] Chen B-C and Lim S-H 2009 *Appl. Phys. Lett.* **94** 171911
[87] Yoshiki K, Hashimoto M and Araki T 2005 *Japan. J. Appl. Phys.* **44** 1066–8
[88] Higgins D A and Luther B J 2003 *J. Chem. Phys.* **119** 3935
[89] Salter P S, Carbone G, Botcherby E J, Wilson T, Elston S J and Raynes E P 2009 *Phys. Rev. Lett.* **103** 257803
[90] Kleman M 1983 *Points, Lines and Walls* (New York: Wiley)
[91] Durrer R, Kunz M and Melchiorri A 2002 *Phys. Rep.* **364** 1–81
[92] Kibble T W B 2003 Symmetry breaking and defects *Patterns of Symmetry Breaking: Proc. NATO Advanced Study Institute* ed A Henryk, D Jacek and W Hubert (Dordrecht, The Netherlands: Kluwer Academic) p 35
[93] Chuang I, Durrer R, Turok N and Yurke B 1991 *Science* **251** 1336–42
[94] Bowick M J, Chandar L, Schiff E A and Srivastava A M 1994 *Science* **263** 943–5
[95] Cladis P E, van Saarloos W, Finn P L and Kortan A R 1987 *Phys. Rev. Lett.* **58** 222
[96] Vella A, Intartaglia R, Blanc C, Smalyukh I I, Lavrentovich O D and Nobili M 2005 *Phys. Rev.* E **71** 061705
[97] Smalyukh I I and Lavrentovich O D 2006 Defects, surface anchoring, and three-dimensional director fields in the lamellar structure of cholesteric liquid crystals as studied by Fluorescence Confocal Polarizing Microscopy *Topology in Condensed Matter* ed M Monastyrsky (Berlin: Springer) pp 205–50
Smalyukh I I and Lavrentovich O D 2003 *Phys. Rev. Lett.* **90** 085503
[98] Engström D, Persson M, Trivedi R P, Bertness K A, Goksör M and Smalyukh I I 2010 *Nat. Mater.* at press
[99] Loudet J C, Barois P and Poulin P 2000 *Nature* **407** 611–3
[100] Anderson V J and Lekkerkerker H N 2002 *Nature* **416** 811–5
[101] Zurek W H 1996 *Phys. Rep.* **276** 177–221
[102] Zapotocky M, Ramos L, Poulin P, Lubensky T C and Weitz D A 1999 *Science* **283** 209
[103] Brasselet E, Murazawa N, Misawa H and Juodkazis S 2009 *Phys. Rev. Lett.* **103** 103903